

A systematic comparison of experimental set-ups for modelling extensional tectonics

Frank Zwaan^{a,b,*}, Guido Schreurs^a, Susanne J.H. Buiter^{c,d},

a) Institute of Geological Sciences, University of Bern, Baltzerstrasse 1+3, CH-3012 Bern, Switzerland

b) Current affiliation: Dipartimento di Scienze della Terra, Università degli Studi di Firenze, Via La Pira, 4, 50121 Florence, Italy

c) Team for Solid Earth Geology, Geological Survey of Norway (NGU), Leiv Eirikssons vei 39, 7040 Trondheim, Norway

d) The Centre for Earth Evolution and Dynamics, University of Oslo, Sem Sælands vei 2A, 0371 Oslo, Norway

Abstract

Analogue modellers investigating extensional tectonics often use different machines, set-ups and model materials, so that direct comparisons of results from different studies can be challenging. Here we present a systematic comparison of crustal-scale analogue experiments using simple set-ups simulating extensional tectonics, involving either a foam base, a rubber base, rigid basal plates or a conveyor base to deform overlying brittle-only or brittle-viscous models. We use X-ray computed tomography (CT) techniques for a detailed 3D analysis of internal and external model evolution.

We find that our brittle-only experiments are strongly affected by the specific set-up, as the materials are directly coupled to the model base. Experiments with a foam or rubber base undergo distributed faulting, whereas experiments with a rigid plate or conveyor base experience localized deformation and the development of discrete rift basins. Pervasive boundary effects may occur due to extension-perpendicular contraction of a rubber base. Brittle-viscous experiments are less affected by the experimental setup than their brittle-only equivalents as the viscous layer acts as a buffer that decouples the brittle layer from the base. Brittle-viscous plate base and conveyor base experiments only localize deformation with high brittle-to-viscous thickness ratios that increases brittle-viscous coupling. This effect is further enhanced by higher strain rates.

Our set-ups are most appropriate for investigating crustal-scale extension in continental and selected oceanic settings. Specific combinations of set-up and model materials may be used for studying young or old regions, or wide or narrow extension. Here, natural factors as temperature variations, extension rate, water content and lithology should be carefully considered. We hope that our experimental overviews may serve as a guide for future experimental studies of extensional tectonics.

1. Introduction

1.1 Analogue experimental set-ups for investigating extensional tectonics

Tectonic analogue modellers have historically used different experimental apparatus and model materials to investigate continental extension. These experiments have provided the scientific community with highly valuable insights in the evolution of basins and initial rift structures. However, a robust comparison between various experiments is challenging, because of the variety of experimental set-ups and model materials that have been used. Experiments have, for example, used set-ups involving (a combination of) basal foam bars, basal rubber sheet, rigid basal plates or conveyor belt style basal sheets with moving sidewalls to deform model materials (e.g. Allemand et al. 1989; Acocella et al. 1999; Bahroudi et al. 2003; Amilibia et al. 2005; Alonso-Henar et al. 2015; Philippon et al. 2015). Alternatively, extension can be achieved through gravitational gliding or spreading, in which case no moving sidewalls or an extending base needs to be applied (e.g. Gartrell 1997; Fort et al. 2004; Acocella et al. 2005). Analogue materials used to simulate brittle parts of the lithosphere include, among others, quartz or feldspar sand, silica flour, microbeads, and (kaolinite) clay (Hubbert 1951, Elmohandes 1981; Serra & Nelson 1988; Clifton & Schlische 2001; Autin et al. 2010; Abdelmalak et al. 2016, Fig.

1). Pure silicone oils and silicone putties are frequently used as analogues for ductile parts of the lithosphere (Basile & Brun 1999; Michon & Merle 2000; Sun et al. 2009, Fig. 1).

Vendeville et al. (1987) present experiments that highlight several factors controlling the geometry of fault systems in extensional tectonics. The study used rubber sheet set-ups with a brittle sand layer for homogeneous thin-skinned deformation, brittle-viscous gravity-spreading models resting on a solid base, and experiments with the whole brittle-viscous lithospheric analogue floating on a simulated asthenosphere (Fig. 1). The results provide a first impression of the differences between these set-ups, revealing the correlation between fault spacing and layer thickness in brittle materials, rift localisation in brittle-viscous settings and isostatic effects, such as tilted margins due to the influence of an asthenosphere (Fig. 1). Yet the many experimental parameters were widely different from experiment to experiment, making a quantitative comparison difficult.

Allemand & Brun (1991) test the influence of material layering, but using a conveyor belt set-up to achieve both symmetric and asymmetric extension with a velocity discontinuity (VD). The basal sheets diverge, representing a fracture in the underlying (not-simulated) brittle lithospheric mantle. Asymmetric extension is shown to generate strongly asymmetric rift geometries, in both brittle and brittle-viscous models. The rifts under symmetric extension conditions also develop a degree of structural asymmetry. Model parameters such as layer thickness, material properties and extension velocities are however not clearly defined, again making ~~again~~ a direct comparison of these experiments challenging.

Brun (1999) summarises extension experiments with a focus on layer rheology and extension velocity. He shows that increasing extension velocities in crustal-scale brittle-viscous conveyor belt models increase viscous strength and brittle-viscous coupling, favouring widespread deformation or wide rifting. By contrast, low extension velocities lead to localized extension or narrow rifting. A similar effect is obtained by changing the brittle-to-viscous thickness ratio: a high ratio of 3:1 leads to high coupling and wide rifting, whereas a small ratio of 1:1 leads to low coupling and narrow rifting. On a lithospheric scale however, the behaviour of the upper mantle becomes important as well (Fig. 1); a single fracture in a strong upper mantle layer may induce narrow deformation in the overlying crustal layers, whereas a weak upper mantle promotes distributed deformation. The models also suggest that within such wide rifts, local weaknesses can account for the development of core complexes. Next to providing a summarizing scheme similar to Brun (1999), Corti et al. (2003) show how magma presence can control graben initiation in narrow rifts and cause a wide rift to shift in core complex mode. The authors also describe the additional effects of oblique extension and multiple extension phases on rift evolution. However, the models presented in both review articles come from numerous studies and are often performed with sometimes very different techniques and parameters.

The additional significance of VDs in the brittle upper mantle was investigated by Michon & Merle (2000; 2003) by means of brittle-viscous base plate experiments, where the VD is situated at the edge of the plate. A single VD leads to asymmetric extension and the development of a single rift, whereas a double VD experiment may form two or more rift basins, depending on the initial distance between the VDs. This is valid for high strain rates, as low strain rates focus deformation (narrow rifting), decreasing the number of rift basins. Apart from the varying strain rates and VDs, the other parameters such as model size, materials and layer thickness remained fixed.

Schreurs et al. (2006) compared results of a brittle-viscous plate base extension experiment that was run by five analogue laboratories. The overall experimental set-up was kept as similar as possible using, for example, the same foil to cover the base of the apparatus, the same extension velocity and the same viscous material (PDMS). But differences occurred in brittle materials (different types of sand and a wet clay) and model width. This study illustrated the overall large-scale structural similarities, but also showed differences in fault dip angle and fault spacing, that were related to differences in model materials and/or model set-up.

1.2 Analogue materials used in extension experiments

Brittle, Mohr-Coulomb type materials have very similar internal friction angles with respect to their natural analogues (ranging between ca. 25° and 40°, Klinkmüller et al. 2016; Schellart & Strak 2016). Granular materials such as dry quartz sand have a very low cohesion and are considered a good analogue for large-scale models aiming at the whole brittle crust or the crust and lithospheric mantle (Fig. 1). By contrast, high-cohesion materials, such as silica flour and clay ($C = 40\text{--}750$ Pa, Eisenstadt & Sims 2005; Guerit et al. 2016), are better suitable for modelling the uppermost kilometres of the crust where cohesion is an important rheological factor. Intermediate cohesions can be obtained by mixing granular materials (Abdelmalak et al. 2016; Montanari et al. 2017). Low-friction microbeads allow the modelling of structural weaknesses or weak crustal lithologies (e.g. Colletta et al. 1991; Panien et al. 2005). The density of brittle analogue materials depends on the specific density, the grain size and handling techniques, as well as water content (for clays), but lies generally between ca. 1400–1800 kg/cm³ (e.g. Krantz 1991; Eisenstadt & Sims 2005; Klinkmüller et al. 2016).

Pure silicone oils consist of polydimethylsiloxane (PDMS), are transparent, have a density of ca. 1000 kg/m³ (Weijermars & Schmeling 1986) and a Newtonian viscosity between c. 10³ Pa·s and 10⁵ Pa·s at room temperature and at typical experimental deformation rates (Rudolf et al. 2015; Schellart & Strak 2016). Silicone putties are mixtures of polyborondimethylsiloxane (PBDMS) and inert fillers (Weijermars, 1986), and have higher densities than pure silicone oils. Examples of opaque silicone putties commonly used in analogue modelling include Rhodorsil Gomme GS1R (Cobbold & Quinquis, 1980), Rhodorsil Silbione 70009 (Nalpas & Brun, 1993) and Dow Corning DC3179 (Dixon and Summers, 1985). Their density range varies between c. 1140 and 1420 kg/m³ and they display Newtonian viscosities between c. 10⁴ and 4·10⁵ Pa·s at room temperature (e.g., Casas et al., 2001; Cagnard et al., 2006; Konstantinovskaya et al., 2007). It should be noted that the viscosity of silicone-based materials can in some cases strongly depend on temperature (Cagnard et al. 2006) and also aging processes have an effect on silicone behaviour (Rudolf et al. 2015 and references therein). Pure silicone oils and silicone putties can be mixed with for instance sand or metallic powders to modify the material's density and viscosity (e.g. Calignano et al. 2015; Zwaan et al. 2016). Other substances, such as paraffin and gelatin mixtures can be applied when power-law or temperature-dependent rheological behaviour is required (e.g. Zulauf & Zulauf 2004; Boutelier & Oncken 2011). In lithosphere-scale models, the weak ductile behaviour of the asthenospheric mantle is simulated with low viscosity materials, such as honey, glucose syrup or even pure water (Mart & Dauteuil 2000; Chemenda et al. 2002; Schellart et al. 2002; 2003; Molnar et al. 2017). These normally exhibit Newtonian behaviour. Further details and references concerning the above-mentioned and other analogue model materials can be found in a comprehensive review article by Schellart & Strak (2016).

1.3 This study

The analogue modelling work summarized above reveals a trend from a rather qualitative modelling approach to a more quantitative approach. Older studies tend to present a range of models with widely different parameters (for materials and set-up), which are often not fully described. By contrast, newer studies often specify such data in much detail, allowing repetition by analogue and also numerical means. Yet direct comparisons between the various methods remains challenging, especially since these methods aim to simulate different tectonic settings (see also sections 2.2 and 2.3). In theory, the scaling principles that have elevated analogue modelling from a qualitative to a quantitative method can be applied to compute how models should compare to each other (e.g. Hubbert 1937; Ramberg 1981; Weijermars & Schmeling 1986). In practice, however, such calculations remain approximate. Different material handling techniques (laboratory traditions, the human factor) or climatic conditions (room temperature, humidity) may influence material behaviour and thus model results with the same set-up can vary from laboratory to laboratory (e.g. Krantz 1991; Schreurs et al. 2006, 2016; Rudolf et al. 2015). Furthermore, our understanding of experimental material rheology may be incomplete or poorly constrained since some parameters are difficult to properly determine (Eisenstadt &

Sims 2005; Dooley & Schreurs 2012). Thus the need for reference studies of lithospheric extension with standardized model parameters remains and to our knowledge no such work is available to date.

The aim of this study is to systematically compare a series of simple crustal-scale, normal-gravity laboratory experiments involving commonly used set-ups and to discuss the tectonic settings to which these would apply. We use either a foam base, a rubber base, rigid base plates or “conveyor belt” style plastic sheets as a mechanism to deform the overlying brittle or brittle-viscous model materials. This forms a total of 8 reference set-ups. Various additional sub-set-ups serve to examine, among others, the effects of varying extension velocity, layer thickness and brittle-to-viscous thickness ratio. We also apply X-ray computed tomography (XRCT or CT) for obtaining a highly detailed 3D view of internal as well as external model evolution.

2. Materials and methods

2.1 Material properties

We ran brittle (single-layer) and brittle-viscous (two-layer) experiments to simulate a brittle upper crust and a complete brittle-ductile crust, respectively (Fig. 2). Reference brittle-only experiments contain a 4 cm thick layer of fine quartz sand ($\phi = 60\text{--}250\text{ }\mu\text{m}$). The sand is sieved from ca. 30 cm height into the experimental apparatus to guarantee a sand density of ca. 1560 kg/m^3 . The sand is flattened using a scraper at every cm thickness during preparation of the experiment, causing slight density variations, which subsequently appears on CT images as a “layering” (Fig. 2f, g). The reference experiments with a brittle-ductile set-up are built of an additional 4 cm thick, near-Newtonian viscous layer (viscosity $\eta = \text{ca. } 1.5 \cdot 10^5\text{ Pa}\cdot\text{s}$; stress exponent $n = 1.05$) consisting of a 1:1 weight mixture of SGM-36 Polydimethylsiloxane (PDMS) silicone and corundum sand ($\rho_{\text{specific}} = 3950\text{ kg/m}^3$, Panien et al. 2006; Zwaan et al. 2016; Carlo AG 2018). The obtained density of the viscous material (ca. 1600 kg/m^3) is close to that of the overlying quartz sand layer (1560 kg/m^3). This results in a density profile that avoids buoyant rise of the viscous material that would occur for pure, low density PDMS ($\rho = 960\text{ kg/m}^3$). Further material properties are listed in Table 1.

2.2. Experimental design

The experimental apparatus consist of a fixed base and two longitudinal sidewalls, which can move outward independently from each other above a fixed support table, controlled by precise computer-guided stepper motors. The initial width of the experiment is 30 cm in all set-ups, which is considerably less than the model length (as specified below). This high length-to-width ratio diminishes the influence of boundary effects of the short sidewalls. Through modification of the apparatus we can use four different methods to transfer deformation from the base of the set-up to the overlying experimental materials: by applying either a foam base or rubber sheet base for a distributed deformation setting, or a base of rigid plates or conveyor belt system for focussed deformation (Fig. 2). The confinement along the short sidewalls varies according to the set-up, as explained below. Since the various set-ups differ significantly, we also specify which type of tectonic setting or crustal rheology is simulated (Fig. 3). An additional overview of the similarities and differences between our set-ups by means of (relative) velocities and shifts in reference frames is provided in Appendix A (Fig. A1).

2.2.1. Distributed deformation set-ups

A foam base (F series experiments) induces distributed deformation (e.g. Schreurs & Colletta 1998; Schlagenhauf et al. 2008; Zwaan et al. 2016, Zwaan & Schreurs 2017). An 8 cm thick RG 50 Polyurethane foam base is first compressed between the sidewalls with the model subsequently constructed on top (Fig. 2a-c). As the sidewalls move apart during an experiment, the foam expands, causing deformation in the overlying materials (Fig. 2b, c). Rubber sidewalls

at the short ends of the set-up confine the materials, with the distributed extension of the rubber decreasing boundary effects there (Fig. 2a). All foam base experiments have a length of 79 cm for an initial length-to-width ratio of 2.6.

For the rubber base set-up (R series experiments) a 1.5 mm thick Neoprene rubber sheet is spanned between the two long sidewalls (e.g. Vendeville et al. 1987; Bahroudi et al. 2003; Bellahsen et al. 2003; Bellahsen & Daniel 2005; Fig. 2d-f). Note that this is slightly different from set-ups applying a rubber sheet between two rigid base plates that are subsequently moved apart (e.g. McClay & White 1995, McClay et al. 2002; Corti et al. 2007; Henza et al. 2010). We use a full rubber base for our experiments in order to allow a comparison with the foam base set-up. When the long sidewalls move apart, the rubber sheet is stretched and extends uniformly with a **constant velocity gradient**, causing distributed deformation (Fig. 2e, f). The sides of the set-up are free, that is, not confined by any sidewall that may influence the experiments, for the experiments with only a brittle layer. The short sidewalls of the brittle-ductile rubber base experiments are enclosed by a sand talus so that the viscous material cannot escape sideways (Fig. 2d). Since the large forces involved in stretching a large rubber sheet may cause damage to the experimental apparatus, the length of the rubber base experiments is kept to 50 cm. Therefore, the initial length-to-width ratio is 1.7.

Previous authors have applied a rubber or foam base with an overlying brittle layer to model distributed thin-skinned extension (e.g. Bahroudi et al. 2003; Schlagenhauf et al. 2008). In nature, distributed extension in the brittle crust could develop in a setting with high brittle-ductile coupling between a brittle upper crust and a strong ductile lower crust (Fig. 3a), either due to high strain rates or high viscosity (Brun 1999, Buiter et al. 2008; Zwaan et al. 2016). Note that the sub-crustal mantle has no influence in this case. By contrast, a set-up with brittle-viscous layers on top of a rubber or foam base would simulate a normal brittle-ductile crust on top of a viscously deforming weak mantle (Fig. 3b). This setting, in which the strength of the lithosphere is determined by the brittle crust (Bürgman & Dresen 2008), can be expected in a hot lithosphere, for instance above a mantle plume (Saunders et al. 1992; Burov et al. 2007) or after a phase of crustal thickening and radiogenic heating (Brun 1999).

2.2.2. Localized deformation set-ups

The plate base set-up (P series experiments) involves two 3 mm thick rigid plastic plates that are fixed to the long sidewalls (Fig. 2g-h) (e.g. Allemand & Brun 1991; Tron & Brun 1991; Brun & Tron 1993; Bonini et al. 1997; Keep & McClay 1997; Michon & Merle 2000). When these plates move apart with the long sidewalls, velocity discontinuities (VD) develop at the basal edges of the plates. The support table below the plates prevents material from escaping (Fig. 2e, f). The short sidewalls are confined by a similar plate system that is fixed to the horizontal plates, thus moving in sync and creating the same boundary conditions as at the base of the apparatus (Fig. 2g). In contrast to the set-ups applying distributed extension described above, the rigid base plates allow both symmetric and asymmetric extension (Fig. 2e, f). In the former case, two moving VD's occur as the edges of both non-overlapping plates move apart, whereas the latter case results in only one VD (similar to Michon & Merle 2000, see also Fig. A1). The initial length of the base plate experiments is 90 cm, so that the length-to-width ratio is 3. Although we did not measure the boundary friction of the plastic plates with quartz sand, it is likely to be close to the values reported by Panien et al. 2006 for plastic and PVC: ca. 20.7°.

The final set-up is a modified version of the plate base set-up involving a "conveyor belt" type of deformation (C series experiments) (e.g. Allemand & Brun 1991; Tron & Brun 1991; Dauteuil & Brun 1993; Keep and McClay 1997; Román-Berdiel et al. 2000). Sub-mm thick plastic sheets or foil ("Alkor" foil 120010 formerly produced by Alkor-Venilia and now available as "Gekkofix 11325" www.gekkofix.com; Klinkmüller et al. 2016) are fixed to the plate base set-up and are led down through a slit in the support table, along the central axis of the experiment (Fig. 2j-l). When the long sidewalls move apart, the sheets are pulled upward through the slit (Fig. 2k, l). In contrast to the plate base experiments, a single VD occurs, which remains located at the centre of the experiment. Since this is true for both symmetrical and asymmetrical experiments

(Fig. 2k, l), the two setups are different. But the asymmetric set-up is, after a switch of reference frame, the same as the asymmetric plate base set-up (Fig. A1) and should thus produce an identical result. The same sheet system is applied on the short sidewalls in order to have a continuous confinement (Fig. 2j). These sheet base experiments have the same length-to-width ratio as the base plate experiments, i.e. 3. The angle of boundary friction of the foil with quartz sand lies between 15° and 21° (Schreurs et al. 2016).

Both the base plate and conveyor base experimental designs involve localized deformation at VD's. These VD's simulate a fault in a strong layer underlying the experimental materials. In the case of our brittle-only experiments, this would translate to a fault at the base of the upper crust. In order to have a fault in the lower crust, the latter needs to behave in a brittle fashion, which in our case would be expected in an old, cool crust (Fig. 3c). On a smaller scale, one can also interpret the VD as a reactivated basement fault affecting overlying strata (e.g. Acocella et al. 1999; Ustaszewski et al. 2005). Concerning our brittle-viscous crustal set-up, the VD translates to a fault in a strong upper mantle (e.g. Allemand & Brun 1991; Michon & Merle 2000). Such a setting can be expected in a young stable lithosphere with a strong brittle mantle (Fig. 3d).

2.3. Additional experimental parameters

For every experimental set-up, we test brittle-only materials and brittle-viscous layering, with a reference layer thickness of 4 cm, so that brittle-only and brittle-viscous experiments are 4 cm and 8 cm thick, respectively. However, for specific experiments, we either apply a 4 cm thick brittle-viscous layering, or we modify the brittle-to-viscous thickness ratio by decreasing the thickness of the viscous layer to 2 or 1 cm, in order to capture the effects that a different crustal layering may have on extensional structures (details in Table 2). This decrease in viscous layer thickness can be either due to a thinner, viscous lower crust, assuming that the brittle crustal thickness remains the same (Fig. 3g, h), or an increase in brittle crustal thickness with a constant Moho depth. In both cases, this would result in a relative strengthening of the lithosphere with respect to the default layering.

We also apply “seeds” to localize deformation in several experiments (Fig. 2, Table 2). These seeds are 1 cm thick, semi-cylindrical viscous rods of the previously described PDMS/corundum sand mixture that are placed at the base of the brittle layer. The seeds are continuous and stretch along the full axis of the experiment. They form weak zones where deformation may localise, since the strong sand cover is locally thinner and thus weaker (e.g. Zwaan et al. 2016). Although we acknowledge that surface processes can influence rift evolution (e.g. Burov & Cloetingh 1997; Bialas & Buck 2009; Zwaan et al. 2017), we neither apply erosion nor sedimentation in our experiments, since we aim to directly evaluate differences in experimental results obtained by differences in simple experimental set-ups.

Our reference extension velocity is 8 mm/h, with both long sidewalls moving 4 mm/h for symmetrical extension, or a single sidewall moving 8 mm/h for asymmetrical extension (Fig. 2). Considering a reference duration of 5 h, the total extension equals 40 mm (or ca. 13%, given an initial width of ca. 30 cm). In addition, we varied extension velocity for selected experiments. In the case of the brittle-only experiments, this should not affect the brittle deformation structures because of the time-independent behaviour of sand. For brittle-viscous experiments however, variations in extension velocity are equivalent to variations in effective linear viscosity and will thus affect the relative strength contrast between the brittle and viscous materials (Fig. 3e, f). In the experiments with a foam or rubber base, a strengthening of the viscous material, due to an increase in extension velocity, translates to a strengthening of the hot lithosphere with increased brittle-ductile coupling but still a relatively weak mantle (compare Fig. 3b with Fig. 3e). In the base plates or conveyor set-up equivalent, a higher extension velocity would then represent a normal crust with increased coupling with respect to the reference settings (Fig. 3f).

A thin (ca. 0.5 mm thick) grid made of dark (corundum) sand with a 4 x 4 spacing applied to the surface of each experiment allows a first-order assessment of surface deformation by means of

top view images, without influencing the experimental results. Furthermore, every component of the machine around the experiment consists of X-ray transparent materials to allow for CT-scanning and various experiments are analysed with CT-techniques to reveal their 3D internal evolution (Fig. 2b). Most experiments marked in Table 2 as “CT-scanned” were a rerun of previous tests performed without CT scanning. Various other experiments were also repeated and did indicate little structural variation, thus good reproducibility is ensured (Table 2, details presented in Appendix B, Figs. B1, B2).

2.4. Scaling

We calculate stress ratios ($\sigma^* = \sigma_{\text{experiment}} / \sigma_{\text{nature}}$) using (Hubbert 1937; Ramberg 1981): $\sigma^* = \rho^* \cdot h^* \cdot g^*$ where ρ^* , h^* and g^* represent the density, length and gravity ratios respectively. The strain rate ratio $\dot{\epsilon}^*$ is derived from the stress ratio σ^* and the viscosity ratio η^* (Weijermars & Schmeling 1986): $\dot{\epsilon}^* = \sigma^* / \eta^*$. The velocity ratio v^* and time ratio t^* can be obtained as follows: $\dot{\epsilon}^* = v^* / h^* = 1/t^*$. Natural values for lower crustal viscosity may have a wide range depending on the specific tectonic setting ($\eta = 10^{19}$ - 10^{23} Pa·s, e.g. Buck 1991; Brun 1999; Bürgman & Dresen 2008). We assume an intermediate lower crustal viscosity of 10^{21} Pa·s, which is in line with recent findings (Shinevar et al. 2015, and references therein). An hour in our experiments thus translates to 0.84 Ma in nature and our reference velocity (8 mm/h) converts to a velocity of ca. 0.5 mm/y in nature, close to typical values for initial continental rifting (1-5 mm/y, e.g. Saria et al. 2014). The scaling parameters are summarized in Table 3.

To ensure dynamic similarity between brittle natural and experimental materials, we calculate the ratio R_s , which is a function of gravitational stress and cohesive strength (C) (Ramberg 1981; Mulugeta 1998): $R_s = (\rho \cdot g \cdot h) / C$. When adapting an intermediate cohesion of ca. 8 MPa for upper crustal rocks, we obtain a R_s value of 67 for both nature and our experiments. This cohesion is relatively low compared to the ca. 20-40 MPa measured for continental rocks (e.g. Handin 1969; Jaeger & Cook 1976; Twiss & Moores 1992), but should be reasonable given that the strength of the earth’s crust is generally reduced due to previous phases of tectonic activity. For viscous materials, the Ramberg number R_m applies (Weijermars & Schmeling 1986): $R_m = \text{gravitational stress} / \text{viscous strength} = (\rho \cdot g \cdot h^2) / (\eta \cdot v)$. Our experimental and the equivalent natural R_m values are the same at 75.

3. Results

3.1. Foam base experiments (F series)

Fig. 4 shows the results of two brittle-only foam base experiments. Experiment F1 (without seed) develops no distinct features except for significant boundary effects along the longitudinal sidewalls towards the end of the experiment (Fig. 4a). In contrast, the seed in experiment F4 localizes deformation in the centre of the experiment, although faulting along the long sidewalls is also visible at the surface (Fig. 4b). The CT data from experiment F4 (with seed) reveals the evolution of these structures in more detail (Fig. 4c-e). After ca. 60 min (8 mm) of extension, a graben starts forming above the seed and becomes visible at the surface after 120 min (16 mm of extension, Fig. 4d, f). This main rift structure continues developing towards the end of the experiment (Figs. 4e, g). The CT images show how additional faulting occurs: first along the sidewalls (Fig. 4d, f), later on throughout the experiment so that at the end of the experiment, pervasive sidewall-parallel striking normal faulting is omnipresent (Fig. 4e, g). Note that this distributed faulting is not visible on the top view images due to the low fault offsets at the surface that do not cast shadows on the model surface (Fig. 4b), and may very well be present in the experiment without seed as well (F1, Fig. 4a). In Experiment F4, the brighter tones at the rift shoulders visualise local uplift: parts of the experiment that are uplifted present less of a barrier to the X-rays since these pass through less material, which shows up

as a brighter colour on CT images. It is however important to stress that these brighter colours do not represent a specific altitude.

The evolution of foam base experiments with a brittle-viscous layering is summarized in Fig. 5. Experiment F5, without a seed, forms no central graben (Fig. 5a). Instead, all deformation is concentrated as boundary effects along the long sidewalls. By contrast, experiment F7, with a seed, produces a well-developed symmetric graben structure. Still also this set-up produces some minor faulting along the long sidewalls (Fig. 5b). CT images illustrate the 3D evolution of experiment F7 (Fig 3c-g). Soon after initiation (30 min, 4 mm extension), a central graben structure with two main boundary faults develops above the seed. As the experiment progresses, this structure continues evolving: the rift basin grows deeper and the brittle material situated between the initial boundary faults starts breaking up due to internal faulting (Fig. 5d, f). Some boundary effects develop, but are relatively minor with respect to the central graben structure (Fig. 5d-g). Towards the end of the experiment the brittle sand is almost breached by the upwelling viscous layer (Fig. 5e g). In this experiment, deformation is strongly focussed on the rift structure and no distributed faulting can be distinguished. As in the brittle-only set-up with a seed (F4), this experiment also develops rift shoulder uplift, as indicated by the bright colours at the model surface (Fig. 5e).

3.2. Rubber base experiments (R series)

The surface evolution of two selected rubber base experiments built of only sand is depicted in Fig. 6. Experiment R1 (Fig. 6a, a') has no seed to localize deformation and, as a consequence, deformation focuses along the sidewalls. In addition, remarkable conjugate faults develop at the end of the experiment (300 min, 40 mm of extension), but are not well visible on the top view images due to poor lighting conditions (Fig. 6a). However, an additional phase of extension (30 min at 40 mm/h) helps to highlight these conjugate faults (Fig. 6a'). In contrast to experiment R1, experiment R5 contains a viscous seed that focuses faulting along the central axis of the experiment (Fig. 6b). As a result, this experiment develops a central graben structure. Similar to experiment R1, well-defined conjugate faults occur as well.

The CT-derived 3D images (Fig. 6c-g) reveal how deformation localizes along the seed and the sidewall in the initial stages of experiment R5, forming a cylindrical rift structure (Fig. 6d). However, after some 20-25 mm of extension, conjugate sets of vertical strike-slip faults start developing (Figs. 6f), which become pervasive toward the end of the experiment (Figs. 6e, g). This curious feature is the result of along-strike compression, as the orthogonally extending rubber sheet contracts perpendicular to the extension direction (Fig. 6a'). Yet the graben structures continue to evolve toward the end of the experiment run (Fig. 6e, g). The brighter colours on the surface seen in Fig. 6g again indicate rift shoulder uplift.

Fig. 7 shows results of four brittle-viscous rubber base experiments. Experiment R7, without seed, produces no clear surface structures except for the strong boundary effects along the sidewalls (Fig. 7a). In contrast, experiment R8, with seed, experiences early fault localization (after 30 min a rift becomes visible at the surface), which continues evolving towards the end of the experiment (Fig. 7b). However, also this experiment develops strong boundary effects along the long sidewalls and at the corners, where some viscous material flows into the gap between the original sand buffer and the retreating sidewalls. The rift structure is best developed in the centre of the experiment and dies out towards the short sidewalls, involving slight block rotation of the sand layer in the four corners of the experiment (Fig. 7b).

Experiment R9 at an increased extension velocity of 80 mm/h (Fig. 7c) produces a central rift that is quite similar to the rift in experiment R8 (Fig. 7b), even though no seed is included. Significantly higher extension velocities (480 mm/h in experiment R10) result in strongly distributed deformation with multiple rifts (Fig 5d). The three experiments without a seed at different extension rates (Fig. 7a, c, d) examine the effect of decreased strength contrast between the brittle and viscous layers. We will discuss this further in discussion section 4.4.

3.3. Plate base experiments (P series)

Experiments P1 and P2 consist of a brittle sand layer on top of plastic-covered rigid base plate(s) (Figs. 1g, 8a, b). In experiment P1 we apply symmetric extension, whereas in experiment P2 extension is asymmetric. Both experiments initially develop a rift above the velocity discontinuity along the central axis of the experiment. However, with continued extension experiment P1 develops a graben with a central horst block in the middle, which does not develop in experiment P2 (Fig. 8a, b). Otherwise, both grabens have the same width. No boundary effects occur along the long sidewalls.

Fig. 8c-g shows the results of the brittle-viscous base plate experiments. Experiments P3 and P7 are following symmetrical and asymmetrical extension, respectively. No seed is included. The structural evolution is similar for both experiments. Rifting initiates at the short sidewalls, where both the base plates and confining plates are moving apart (Figs. 1h, 8c, d). These rifts propagate slightly towards the centre of the experiment, but strong boundary effects along the long sidewalls take up much of the extension there and no continuous rift structure develops in the centre of the experiment (Fig. 8c, d). As a result, block rotation takes place on both sides of the propagating rifts. The surface structures are largely the same in both experiments, suggesting that the application of symmetric or asymmetric extension does not have a significant influence in this set-up.

The application of a seed on top of the viscous layer (Exp. P10, in symmetric extension) results in early localization and rift development along the central axis of the experiment (Fig. 8e). This structure continues developing throughout the experiment, yet more extension is accommodated towards the short sidewalls than the middle section, where boundary effects along the long sidewalls take up a larger part of the deformation, similar to experiments P3 and P7 (Fig. 8c, d).

The thick viscous layer in experiments P3 and P7 likely dampens the influence of the basal boundary condition on the sand layer. We therefore run further tests with half the layer thickness for the viscous material, keeping the same brittle-to-viscous ratio (2 cm brittle and 2 cm viscous material, without seed). These experiments did not produce a continuous graben structure either. However, experiment P9, with a higher 80 mm/h extension velocity (and again 2 cm brittle and 2 cm viscous layers, without seed), produces interesting basin geometries (Fig. 8f, g). Instead of developing a simple rift structure, the viscous layer at the centre of the experiment is strongly stretched, creating a depression with continuous rift basins at its margin due to what seems to be passive downbending (Fig. 8g). Secondary graben structures develop further away from the central depression, indicating a degree of distributed deformation. Notably, no boundary effects occur along the long sidewalls, in contrast to the other brittle-viscous plate base experiments.

3.4. Conveyor base experiments (C series)

Fig. 9 shows the results of the conveyor base set-up with only a brittle layer (experiments C1 and C3). Both experiments develop a large rift structure along the central axis of the experiment (Fig. 9a, b), rather similar to the plate base experiments P1 and P2 (Fig. 8a, b). We do, however, not observe a difference between the symmetrical and asymmetrical set-ups.

The results of the brittle-viscous experiments show more diversity than their brittle-only counterparts (Fig. 9c-g). Experiment C4, with symmetrical extension, develops two rifts that originate from the short sidewalls and propagate towards the experiment centre (Fig. 9c). They do however not connect, as boundary effects along the long sidewalls take up most of the deformation in the centre, similar to the structures observed in the plate base equivalents (experiments P3 and P7, Fig. 8c, d). We did not run an asymmetrical extension experiment. Instead, we attempted to reduce the boundary effects along the short sidewalls by applying lubricants or adding a sand buffer as proposed by Tron & Brun (1991) (experiments C5 and C6,

respectively). Unfortunately, the boundary effects remained or got worse (See Appendix B, Fig. B1). Furthermore we ran the conveyor base equivalent of experiment P9 (2 cm sand, 2 cm viscous material, Fig. 8f, g), labelled C12, with very similar results to experiment P9 (Fig. B2).

We also tested the effect of decreasing viscous layer thickness, thus increasing the brittle-to-viscous ratio, in experiments C7 and C8. In experiment C7 (Fig. 9d), the thickness ratio is 2, which does not lead to a significantly different structural evolution compared to the reference setup of experiment C4 (Fig. 9c). However, decreasing the viscous layer thickness further to 1 cm (ratio: 4), leads to localization of faulting along the central axis of the experiment during early stages of the experiment, whereas rifting becomes more widespread towards the end of the experiment (C8, Fig. 9e). Tests with higher extension velocities (80 and 40 mm/h for experiments C9 and C10/C11, respectively, see Table 2 and Appendix B, Fig. B2) have shown to improve rift localization, and one such experiment was run in a CT scanner (experiment C11, Fig. 9f, g). These experiments all develop the same features: a double rift system on either side of the VD, which internally grows more complex with time. We also observe the development of further, minor additional rift basins striking parallel. Slight boundary effects occur along the long sidewalls in experiments C10/C11 as well (Fig. 9f, g).

4. Discussion

4.1. General structures

We present a schematic overview of our experimental results in Fig. 10, summarizing the general structures in map view and section, and Table 4, linking these observation with potential natural settings. A clear distinction exists between the brittle-only experiments (left-hand half of upper three rows in Fig. 10) and the brittle-viscous experiments (right-hand half of upper three rows in Fig. 10) since the viscous layer acts as a buffer between the deformation-inducing base and the overlying sand. In the brittle-only experiments, no such buffer exists and deformation induced by the model base is directly transmitted to the overlying sand cover, leading to more distinct structural differences between the experimental series. In addition, the bottom row of Fig. 10 summarizes the structures observed in the high extension velocity experiments and the tests with high brittle-to-viscous ratios. Our experimental results are discussed in more detail below.

4.2. Brittle-only experiments

In the foam base experiments, the sand above the foam directly experiences the distributed deformation induced by the expanding foam, causing fault development throughout the experiment, but mainly along the long sidewalls (Figs. 4a, 10a). Schlagenhauf et al. (2008) report similar but more pronounced distributed rifting, possibly enhanced by a higher degree of extension of their foam base (20% vs. our 13%) and a thicker sand pack (8 cm vs our 4 cm). Seeds do localize rift basins in our experiments, but these structures only account for a minor part of the extension as the rifts experience little subsidence with respect to most other experiments (e.g. P1 and P2 in Figs. 8a, b). The brittle-only rubber base experiments produce similar structures to the brittle-only foam base experiments: distributed deformation and a minor axial rift when a seed is applied (Fig. 6). Significant faulting develops at the long sidewalls and migrates towards the centre of the experiment (Fig. 6c-g), which could be explained by stronger strain gradients in the rubber near the sidewalls (Ackermann 1997). A similar effect could possibly occur in the foam base experiments as well, explaining the comparable boundary effects.

The rubber base experiments also develop conjugate strike-slip faults due to the contraction of the rubber perpendicular to the extension direction (Poisson effect) (Smith & Durney 1992; Venkat-Ramani & Tikoff 2002). Such structures are not always observed in other model studies

applying a rubber base set-up (e.g. Vendeville et al. 1987, Fig. 11a). The Poisson effect-related structures we obtain are probably due to the relatively low length-to-width ratio rubber base we use (ca. 1.7). Rubber base models by McClay & White (1995) and McClay et al. (2002) with much higher length-to-width ratios (6 and 4, respectively) do not undergo any visible contraction perpendicular to the extension direction, whereas an experiment by Bahroudi et al. (2003) with a length-to-width ratio of 0.8 develops strong conjugate faulting (Fig. 11b). The faults in Bahroudi et al. (2003) have a normal fault component as well, possibly because the rubber was stretched from one side only. It is furthermore interesting to note that the Poisson effect may occur in very different types of models or materials. Chemenda et al. (2002) for instance, applying an elasto-plastic mixture of various components floating on water to simulate the lithosphere and asthenosphere, also obtain pervasive conjugate faults due to extension-perpendicular contraction.

Contrary to their rubber and foam base equivalents, a strong localization of faulting above the velocity discontinuity (VD) occurs in the brittle-only plate base and conveyor base experiments (Figs. 8a, b, 9a, b, 10i, j). The plates and sheets translate overlying materials, except at the velocity discontinuity, where extension localises and deep rift basins form. The centre of the rift basins in both the asymmetric and symmetric experiments lies practically at the same level as the experimental base at the end of the experiment (4 cm depth, scaling to a 20 km deep basin in nature, Fig 8i, j). In nature, isostatic compensation would have reduced basin depth. These set-ups may therefore perhaps best be used for investigating initial (small) amounts of extension (e.g. maximum half the thickness of the brittle crust), or larger amounts of extension when significant sedimentation is applied (e.g. Allemand & Brun 1991; Brun & Tron 1993; Keep & McClay 1997). The small horst structure along the axis of the symmetric extension plate base experiment (Figs. 8a, 10i) is likely formed when both plates move away, leaving a small quantity of material behind in the middle. Previous authors have shown the impact extension asymmetry can have on rift geometry by creating strongly asymmetric graben structures (Allemand et al. 1989; Allemand & Brun 1991; Panien et al. 2005, Fig. 11c, d). Yet these effects are not directly observed in our experiments, possibly due to the relatively minor total extension, the lack of syn-rift sedimentation or because we lack the necessary cross-sections as these models were not CT-scanned.

4.3. Brittle-viscous experiments

The presence of a viscous layer in our experiments leads to quite different structures with respect to those observed in their brittle-only counterparts (Fig. 10). The brittle-viscous foam and rubber base cases produce basically the same structures: when no seed is present, faulting occurs only along the sidewalls, whereas a seed concentrates deformation, resulting in a central rift structure (Figs. 5a, b, 7a, b, 10c, d, g, h). The decoupling from the foam or rubber base allows the brittle cover to behave as rigid blocks, more or less passively floating on the viscous layer (Zwaan et al. 2017), whereas the sand in the brittle-only experiments is directly coupled to the base, forcing a pervasive type of faulting (Fig. 10a, b, e, f). Due to this decoupling effect of the viscous layer, no conjugate strike-slip fault sets occur in the brittle-viscous rubber base experiments, similar to the experiments of Bellahsen et al. (2003). The fact that the rifts in our rubber base experiments are less developed towards the short ends of the set-up is most likely caused by the use of a sand talus to contain the viscous material there (Figs. 2d, 6, 7b-d). This creates a deformation contrast between the immobile talus and the deforming material above the rubber sheet, an effect that could potentially be reduced by using a rubber sidewall, as in the foam set-up (Fig. 1a).

In contrast to the brittle-only experiments, the results of the brittle-viscous plate base and conveyor base experiments are quite similar to their foam and rubber base equivalents (Fig. 10), most likely due to the tendency of the viscous material to easily spread out when subject to extension. All of these experiments, however, see minor rifting initiating at the short sides of the set-up, because there the model is confined by sidewalls or sheets that move in sync with the long sidewalls, imposing the same boundary conditions there as at the base of the set-up. The resulting additional drag enhances the extensional deformation at these short edges, forcing

the development of rifts, which propagate toward the centre of the experiment (Figs. 8c-e, 9c, d, 10k). In the centre, however, the viscous spreading mechanism is dominant, so that we observe the same structures as in the other brittle-viscous experiments (Fig. 10). This “short sidewall effect”, which is also present when applying a seed, causing the rifts to be more developed at the short ends of the experiment (Figs. 8e, 10l), may also have occurred in a model by Mart & Dauteuil (2000). Their experiment involves a curious propagating rift system, initiating at the short edge of the set-up, which has a similar plate confinement as in our experiments. In order to reduce this type of boundary effects, higher strain rates can be applied (Fig. 9). The use of a sand talus to confine the short ends of the experiment as suggested by Tron & Brun (1991) does not reduce these boundary effects in our experiments, as the sand has an even stronger rigid relation to the experimental materials as the side plates (or sheets) (experiment C5, Appendix B2).

As with the reference brittle-only experiments, we do not observe a clear difference between symmetric and asymmetric extension on the scale of our set-ups. Yet previous authors have shown that asymmetric extension may have an effect in brittle-viscous settings as well. This is however mostly in combination with a relatively thin viscous layer that enhances brittle-viscous coupling (e.g., Allemand et al. 1989). By contrast the relatively thick viscous layer in our reference models acts as a buffer, decoupling the sand from the asymmetrically extending plates or sheets (see also section 4.5).

4.4. Velocity effects: wide rifting versus passive downbending and marginal basin formation

As discussed in section 4.2, the brittle-viscous foam and rubber base experiments without a seed lack the brittle-viscous coupling necessary to transfer deformation to the brittle layer. Stronger coupling can be achieved by either using a material with a higher viscosity or by increasing the extension velocity (which effectively increases viscosity) as in experiments R9 and R10 (Fig. 7c, d). A higher viscosity would allow the transfer of distributed extension applied by the base to the brittle layer and thus lead to distributed or wide rifting (Brun 1999; Buiter et al. 2008; Zwaan et al. 2016; Figs. 7c, d, 10m, m'). Note that the central rift in experiment R9 is not localized by a seed (Fig. 7c), but probably forms due to some wide rifting effect: the higher the extension velocity (while keeping all other parameters constant), the higher the brittle-viscous coupling and the more rifts develop, as illustrated by experiment R10 (Fig. 7d). Still the type of deformation in these experiments is not as evenly distributed as in their brittle-only equivalents (Figs. 4, 10a, a', b, b', e, e', f, f'), probably since brittle-viscous coupling is not high enough.

Considering the results from the high velocity rubber base experiments R9 and R10 (Fig. 7c, d, 10m, m'), those of the high velocity brittle-viscous plate/conveyor base experiments P9 (Fig. 8f) and C12 (Fig. B2) may seem somewhat remarkable; instead of developing distributed rifting, these models generate a ‘down-bent’ depression bordered by marginal grabens (Figs. 8f, g, 10n, n', B2). It seems that the high extension velocity in P9 and C12 (80 mm/h, translating to 320 mm/h for the reference layer thickness) causes high coupling between the viscous layer and the brittle cover, as well as between the viscous layer and the base. The set-ups lead to intense stretching (necking) above the VD(s) and subsequent downward ‘bending’ of the sand cover (Fig. 8g). High coupling between the viscous layer and the base also explains why no apparent boundary effects are visible along the longitudinal sidewalls. The bending of the brittle layer at the edge of the system causes local extension in the sand and the formation of marginal basins. Similar structures can be observed along the Western Escarpment of the Afar (northernmost sector of the East African Rift System) in Ethiopia (e.g. Abbate & Sagri 1969; Chorowicz et al. 1999), possibly caused by loading and bending due to massive diking and underplating in the adjacent rift basin (Corti et al. 2015). Our experiment may suggest that rapid extension of the crust could also cause such basin geometries.

4.5. Effects of different brittle-to-viscous ratios

Our brittle-viscous plate and conveyor base set-ups with the reference brittle-to-viscous thickness ratio fail to produce proper rift basins, in contrast to their brittle-only equivalents (experiments P1, P2, C1 and C2, Figs. 8a-d, 9a,b, 10k). Instead, we either need a seed as in the foam and rubber base experiments (experiment P10, Figs. 8e, 10l), or a high brittle-to-viscous thickness ratio (>2) to localize deformation (experiments C8 and C11, Fig. 9e-g). In the latter case, high extension velocities improve localization (experiment C11, Fig. 9f, g). Yet we obtain double rift structures rather than the single rift basins in the brittle-only experiments.

Also Tron & Brun (1991) apply a relatively thin viscous layer (brittle-to-viscous ratio of ca. 2) and obtain well-developed rift structures in symmetric extension (Fig. 11f). The thin viscous layer probably increases brittle-viscous coupling, causing the experimental brittle materials to behave as rigid blocks and leading to rift localization near the VD, similar to our brittle-only experiments (Fig. 8a, b, 9a, b). The extension model by Tron & Brun (1991, Fig. 11f) produces the same double rift structure including the additional faults away from the central rifts as our experiment C11 (Fig. 9f, g). Also Keep & McClay (1997) and Schreurs et al. (2006) obtain two rifts with symmetrical extension experiments involving a conveyor or plate base and a brittle-to-viscous ratio of 4 and 6, respectively. A lateral transfer of deformation through the viscous layer, away from the VD is the probable cause of this dual rift arrangement (Michon & Merle 2000; 2003, Fig. 11e). This feature seems to occur in asthenospheric-scale models as well (Vendeville et al. 1987, Fig. 1). A single rift structure may form due to factors as higher strain rates (Keep and McClay 1997; Michon & Merle 2000), asymmetric extension or possibly syn-rift sedimentation (e.g. Brun & Tron 1993, Fig. 11f). The formation of a single or dual rift structure is most likely influenced by the viscosity of the viscous layer as well. Experiments with high brittle-to-viscous ratios thus seem to be highly sensitive to various parameters. Whether the various viscous layer thickness ratios mentioned above are realistic depends on the specific tectonic setting that is simulated, as lithospheric rheological profiles are known to vary considerably in extensional settings (e.g. Brun 1999; Burov 2011; Tetreault & Buiter 2017, see also section 4.7).

4.6. Boundary conditions and boundary effects

Most of our reference experiments, except for the brittle-only plate and conveyor base experiments, develop some degree of normal faulting along the long sidewalls (Fig. 10). In the brittle-only experiments, this may be due to enhanced local stretching of the rubber base (Ackermann 1997), an effect possibly present in the foam base equivalents as well. The rigid sand layer in the brittle-viscous experiments on the other hand is subject to “inertia”, i.e. an inability to move and extend as easily as the viscous materials, leaving “gaps” along the sidewalls that take up significant amounts of deformation in the experiment (Zwaan et al. 2017).

Some authors avoid this “inertia” effect by simply ignoring it and focussing on the structures in the centre of the experiment. Others attempt to reduce faulting by applying a viscous layer that does not reach the model sidewalls (Tron & Brun 1991; Schreurs et al. 2006). By narrowing the viscous layer however, the boundaries of the viscous material become rheological contrasts that may trigger faulting themselves, thus causing a new type of boundary effects (e.g. Bonini et al. 1997). This also raises the question what the viscous layer represents in nature, if not a continuous viscous lower crust. Even narrower patches of viscous material, for instance simulating a weak zone in the crust due to magmatism, lead to narrower rift structures (e.g. Brun & Nalpas 1996; Dauteuil et al. 2002) and the seeds in our experiments can be seen as the most extreme exponent of this trend. The width of the structural weakness is also relevant for set-ups involving a rubber base fixed between two base plates (e.g. McClay & White 1995, McClay et al. 2002; Corti et al. 2007; Henza et al. 2010). In such experiments, all deformation occurs above the rubber sheet, with its edges acting as the boundaries of the rift system.

Our results show that the type of confinement along the short edges of the brittle-viscous experiment forms another important factor generating boundary effects. In the foam base

experiments, the rubber sheet sidewalls cause little to no additional deformation, yet the sand talus confinement in the rubber base experiments generates significant boundary effects, and enhanced rifting is associated with the plate base and conveyor base confinements. However, the similarity of the structures in the centre of all our reference brittle-viscous experiments (due to the likely dominance of the viscous spreading mechanism under low brittle-viscous coupling conditions) may suggest that, if the short edge boundary effects can be reduced, the type of extension mechanism would be of little influence under our standardized conditions. Therefore we could perhaps have obtained comparable results for brittle-viscous set-ups even without a method to induce deformation directly at the base of the experimental materials: only moving apart the two longitudinal sidewalls may suffice to cause uniform spreading of the viscous layer (e.g. Le Calvez & Vendeville 2002; Autin et al. 2010, 2013; Marques 2012). However, the results of such experiments may again vary with different strain rates, layering and layer thickness, materials, application of sedimentation etc., highlighting the challenges of directly comparing the results from different modelling studies and the need to specify all relevant parameters and boundary conditions, as well as any resulting boundary effects.

4.7. Recommendations for extension experiments

Our extension experiments represent different rheological stratifications and extension conditions (Fig. 3), which may serve as a guide for other modelling studies aiming at investigating extension in specific tectonic settings. We calculated a series of rheological profiles for natural cases to allow a direct rheological comparison to the analogue set-ups (Fig. 12). We used the rheological values of Table 3 with laboratory flow laws often used for the lower crust and lithospheric mantle (Hirth & Kohlstedt 2003; Rybacki et al. 2006). We varied extension velocity (0.5 to 10 mm/yr) and Moho temperature (550 and 650 °C). The calculations show that extension velocity has a relatively minor influence on the rheological profile with respect to temperature and dry or wet versions of the flow laws. The plots also indicate that our reference brittle-to-viscous ratio of 1:1, although often used in analogue models (Corti et al. 2003 and references therein), is quite low (compare Fig. 12a, with Fig. 12b) and may only occur in a relatively wet and hot lithosphere (Fig. 12f). This may for instance be in accordance with the situation in the East African Rift System (Fadaie & Ranalli 1990; Corti 2009), but a 2:1 or 3:1 ratio would fit better with the calculations for a normal-temperature lithosphere (Fig. 12b-d). A strong upper mantle, as inferred for (brittle-viscous) plate and conveyor base set-ups, only occurs in a wet cold lithosphere (Fig. 12) or in a completely dry lithosphere (dotted lines in Fig. 12), yet the complete absence of hydrous minerals may be unrealistic (Xia & Hao 2010). Note, however, that our strength profile calculations are based on monomineralic flow laws (anorthosite and olivine, Hirth & Kohlstedt 2003; Rybacki et al. 2006), whereas continental rocks are of course polymineralic. Different rheological profiles for natural settings can be obtained by not only varying the thermal gradient, but also by variations in water content, temperature or by simply using other flow laws. We choose lower crust and mantle flow laws (Rybacki et al. 2006 and Hirth & Kohlstedt 2003, respectively) that are fairly recent and neither overly weak nor strong in comparison with other flow laws.

The rheological calculations highlight that one should carefully consider the various factors that may influence the strength of the lithosphere in a given tectonic setting before selecting a specific experimental set-up. It is also important to stress that although the materials involved may only represent the upper parts of the crust, deeper parts of the lithosphere (basement or mantle) are simulated via the chosen experimental extension mechanism (Fig. 3). This is most evident for brittle-only models that are directly coupled to the set-up (Fig. 10). However, we have shown that for low extension velocity brittle-viscous experiments, that aim at representing a hot lithosphere, any extension mechanism should suffice due to the high degree of decoupling (Fig. 10). This decoupling effect could also allow a simple way to model an oceanic lithosphere, which is generally considered to comprise a brittle oceanic crust and a viscous lithospheric mantle (e.g. Benes & Scott 1996). Note, however, that in such set-ups an imposed weakness is necessary to create any rift structure at all (Fig. 10). Since efforts should be made to keep boundary effects to a minimum, we recommend using the foam base method for such brittle-viscous models (see also section 4.6).

Our set-ups could be extended to include more layers (three or four-layer lithospheres) (e.g. Corti et al. 2003) and an underlying asthenosphere, that would allow an assessment of the effect of isostatic compensation on a stretching lithosphere. In such set-ups, a strong lithosphere would strongly affect rifting processes (Brun 1999; Corti et al. 2003), whereas in the case of a weak lithosphere (Figs. 3b, e, 12b-d, g, h), the (rising) asthenosphere may have an important impact. The presence of an asthenosphere analogue would also allow the vertical motions associated with a major fault or shear zone in the strong upper mantle (e.g. Vendeville et al. 1987, Fig. 1). In the commonly used plate and conveyor base set-ups such a fault is represented by the VD, yet any associated vertical motions are not simulated. The conveyor belt extension mechanism may not be well suited to crustal-scale models, as the continuous “upwelling” of the plastic sheets resembles a convection cell system, which could be taken to simulate sub-lithospheric mantle behaviour. **The conveyor base set-up would therefore be more appropriate for lithospheric-scale models.** For crustal-scale wide rift experiments we recommend using a plate base set-up.

It could also be worthwhile to repeat our experiments with other brittle materials and viscous analogues, which may better capture the behaviour of the lithosphere (overview in Schellart & Strak 2016). The use of temperature-dependent materials would allow the inclusion of temperature effects (e.g. Boutelier & Oncken 2011), which can strongly control rifting as shown by numerical simulations (Tetreault & Buiter, 2017). Furthermore, a **next necessary step** in modelling rift structures is to include surface processes as well (e.g. Burov & Cloetingh 1997; Bialas & Buck 2009; Zwaan et al. 2017).

We would like to stress the importance of standardized modelling methods and strict lab procedures (e.g. Klinkmüller et al. 2016). Different handling techniques, laboratory conditions and personal preferences may cause variations in, for instance, sand density (e.g. Krantz 1991) or rheology of viscous materials (Rudolf et al. 2015) and can have significant effects on model results (Schreurs et al. 2006, 2016). By means of standardized procedures within a modelling group, these variations can be reduced. Yet reproducing the same model results in different laboratories will probably always remain a challenge (see efforts by Schreurs et al. 2006, 2016).

5. Conclusion

We presented a systematic comparison of four setups commonly used for analogue modelling of crustal-scale extension. We examined distributed extension obtained by a foam or rubber base and localised extension by rigid basal plates or conveyor-belt basal sheets. We find that:

1. Brittle-only experiments are strongly affected by the experimental setup, as the materials are directly coupled to the base of the set-up. Foam base or rubber base experiments therefore undergo distributed deformation and wide rifting, whereas plate base or conveyor base experiments experience localized deformation and narrow rifting.
2. Strong boundary effects may occur due to extension-perpendicular contraction effects during stretching of a rubber base (Poisson effect, e.g. Smith & Durney 1992). This may be mitigated by using a high length-to-width ratio for rubber base set-ups.
3. Brittle-viscous experiments are less affected by the experimental setup than brittle-only equivalents as the viscous layer acts as a buffer that decouples the brittle parts from the base of the set-up.
4. Of the brittle-viscous experiments we tested, the least boundary effects occur for a setup involving a foam base and a stretchable rubber sidewall. This sidewall method could also be applied to a rubber base setup to minimize boundary effects. In contrast, the plate base and conveyor base set-ups may experience major boundary effects along their short sidewalls that may prove difficult to mitigate.
5. The poor rift development in our reference brittle-viscous plate base and conveyor base experiments is linked to relatively low brittle-to-viscous thickness ratio and strain rates.

Apart from inserting a structural weakness in the sand, we achieve better localization with higher brittle-to-viscous ratios and higher strain rates, which increase brittle-viscous coupling. High strain rates with reference brittle-to-viscous ratios can also cause intense stretching of the viscous layer and downbending effects, leading to the formation of basins with marginal grabens.

The significant differences between experimental results obtained with the different set-ups, sometimes due to seemingly small differences in, for instance extension velocity or layer thicknesses, indicate the need to accurately specify model parameters and boundary conditions in order to allow meaningful comparisons between (analogue) modelling studies. The combination of rheological stratification and experimental set-up defines the tectonic setting that is investigated. Our set-ups can be applied to study extension of crustal materials in young, weak or old, strong lithospheres with different levels of basement control. Here factors as temperature, extension rate, water content and lithology should be taken into account (Fig. 12). We advise to avoid the conveyor belt method for crustal-scale models.

Finally we recommend that every laboratory standardize its procedures and methods as much as possible in order to minimize variations due to different handling techniques and personal preferences.

6.1. Appendix A. Schematic overview of relations between experimental set-ups

Fig. A1 provides an overview of the various set-ups and how these compare to each other by means of extension velocities and shifts of reference frames. All symmetric extension set-ups are different: foam/rubber base experiments (Fig. A1a, b) develop an extension gradient, whereas the plate and conveyor base experiments develop velocity discontinuities (Fig. A1d, e and i, j, respectively). Also the plate and conveyor set-ups are different (e.g. a moving and fixed VD occurs in plate base and conveyor base configurations, respectively, as is revealed after applying a shift of reference frame, Fig A1e, j). Asymmetric extension set-ups differ from their symmetric equivalents as well, but are between themselves, after a shift of reference frame, basically the same (Fig. A1g, l).

6.2 Appendix B. Experimental reproducibility

Figs. B1 and B2 show the surface results of repeated experiments in order to evaluate their reproducibility. In most cases, the structures are very similar. Although the boundary effects in P6 and P7 (Fig. B1) do show some variation, the structures in the centre are the same in both cases (no rift). Experiments C4-C6 seem quite different (Fig. B1), but C5 and C6 are tests to reduce boundary effects. As proposed by Tron & Brun (1991), we added sand to confine the short ends of the experiment, but instead of improving the situation this measure increases boundary effects. In C6 (Fig. B1) we added a lubricant (hand soap) between the sides and the model. Since there was no improvement, we aborted the experiment after 120 min. Note that asymmetric brittle-viscous plate base experiment P6 and symmetric brittle-viscous conveyor belt experiment C4 are quite similar, due to viscous decoupling effects. Also asymmetric brittle-only plate/conveyor base experiments P2, C2 and C3 produce the same structures (Fig. B2), since both the plate base and conveyor base set-ups are, after a shift of reference frame, identical in asymmetric extension conditions. The double rift structure in conveyor base experiment C10 is almost identical to the version generated in C11 (Fig. B2), although the curving nature of the normal faults does provide local variations in rift width. High-velocity models P9 and C12 develop very similar structures, although those in the conveyor belt set-up (C12) are better developed than in plate base experiment P9 (Fig. B2). Note that the additional rift basins in C12 are also present in P10, but not very visible due to their less evolved state and the unfavourable lighting conditions.

7. Author contribution

The first author, Frank Zwaan, performed the analogue models and composed the first version of the manuscript. Second author and project supervisor Guido Schreurs assisted with the model interpretation and the finalizing of the manuscript. This study was inspired by a collaboration on numerical-analogue comparisons with third author Susanne Buitter, who helped planning and discussing the model series, provided a comparison to natural strength profiles, and helped in finalizing the manuscript.

8. Acknowledgements

We would like to express our gratitude to Nicole Schwendener for assisting us with the CT-scanning, Marco Herwegh for providing the necessary financial support to upgrade the experimental apparatus and to the engineers from IPEK Rapperswil (Theodor Wüst, Reto Gwerder, Rudolf Kamber, Michael Ziltener and Christoph Zolliker) for realizing these improvements. We thank John Naliboff and Jürgen Adam for supportive discussions and testing of analysis techniques. This project was funded by the Swiss National Science Foundation (grant no. 200021_147046/1).

References

- Abbate, E., Sagri, M. 1969. Dati e considerazioni sul margine orientale dell'altopiano etiopico nelle province del Tigray e del Wollo. *Bollettino della Società geologica italiana* 88, 489–497.
- Abdelmalak, M.M., Bulois, C., Mourgues, R., Galland, O., Legland, J.-B., Gruber, C. 2016. Description of new dry granular materials of variable cohesion and friction coefficient: Implications for laboratory modeling of the brittle crust. *Tectonophysics* 684, 39-51.
<https://doi.org/10.1016/j.tecto.2016.03.003>
- Ackermann, R.V. 1997. Spatial distribution of rift related fractures: field observations, experimental modelling, and influence on drainage networks. Unpublished PhD thesis, Rutgers University.
- Acocella, V., Faccenna, C., Funiciello, R., Rossetti, F. 1999. Sand-box modelling of basement-controlled transfer zones in extensional domains. *Terra Nova* 11 (4), 149-156.
<https://doi.org/10.1046/j.1365-3121.1999.00238.x>
- Acocella, V., Morvillo, P., Funiciello, R. 2005. What controls relay ramps and transfer faults within rift zones? Insights from analogue models. *Journal of Structural Geology* 27, 397-408.
<https://doi.org/10.1016/j.jsg.2004.11.006>
- Allemand, P., Brun, J.-P., Davy, P., Van der Driessche, J. 1989. Symétrie et asymétrie des rifts et mécanismes d'amincissement de la lithosphère. *Bulletin de la Société Géologique de France* 8 (3), 445-451.
<https://doi.org/10.2113/gssgfbull.V.3.445>
- Allemand, P., Brun, J.-P. 1991. Width of continental rifts and rheological layering of the lithosphere. *Tectonophysics* 188, 63-69.
[https://doi.org/10.1016/0040-1951\(91\)90314-I](https://doi.org/10.1016/0040-1951(91)90314-I)
- Alonso-Henar, J., Schreurs, G., Martinez-Díaz, J.J., Álvarez-Gómez, J.A., Villamor, P. 2015. Neotectonic development of the El Salvador Fault Zone and implications for the deformation in the Central America Volcanic Arc: Insights from 4-D analog modeling experiments. *Tectonics* 34, 133-151.
<https://doi.org/10.1002/2014TC003723>
- Amilibia, A., McClay, K.R., Sàbat, F., Muñoz, J.A., Roca, E. 2005. Analogue Modelling of Inverted Oblique Rift Systems. *Geologica Acta* 3 (3), 251-271.
<https://doi.org/10.1344/105.000001395>
- Autin, J., Bellahsen, N., Husson, L., Beslier, M.-O., Leroy, S., d'Acremont, E. 2010. Analog models of oblique rifting in a cold lithosphere. *Tectonics* 29, TC6016.
<https://doi.org/10.1029/2010TC002671>
- Autin, J., Bellahsen, N., Leroy, S., Husson, L., Beslier, M.-O., d'Acremont, E. 2013. The role of structural inheritance in oblique rifting: Insights from analogue models and application to the Gulf of Aden. *Tectonophysics* 607, 51-64.
<https://doi.org/10.1016/j.tecto.2013.05.041>
- Bahroudi, A., Koyi, H.A., Talbot, C.J. 2003. Effect of ductile and frictional décollements on style of extension. *Journal of Structural Geology* 25, 1401-1423.
[https://doi.org/10.1016/S0191-8141\(02\)00201-8](https://doi.org/10.1016/S0191-8141(02)00201-8)
- Basile, C., Brun, J.-P. 1999. Transtensional faulting patterns ranging from pull-apart basins to transform continental margins: an experimental investigation. *Journal of Structural Geology* 21, 23-37.

- [https://doi.org/10.1016/S0191-8141\(98\)00094-7](https://doi.org/10.1016/S0191-8141(98)00094-7)
- Bellahsen, N., Daniel, J.-M., Bollinger, L., Burov, E. 2003. Influence of visous layers on the growth of normal faults: insights from experimental and numerical models. *Journal of Structural Geology* 25, 1471-1485.
[https://doi.org/10.1016/S0191-8141\(02\)00185-2](https://doi.org/10.1016/S0191-8141(02)00185-2)
- Bellahsen, N., Daniel, J.M. 2005. Fault reactivation control on normal fault growth: an experimental study. *Journal of Structural Geology* 27, 769-780.
<https://doi.org/10.1016/j.jsg.2004.12.003>
- Benes, V., Scott, S.D. 1996. Oblique rifting in the Havre Trough and its propagation into the continental margin of New Zealand: Comparison with analogue experiments. *Marine Geophysical Researches* 18, 189-201.
<https://doi.org/10.1007/BF00286077>
- Bialas, R.W., Buck, W.R. 2009. How sediment promotes narrow rifting: Application to the Gulf of California. *Tectonics* 28, TC4014.
<https://doi.org/10.1029/2008TC002394>
- Bonini, M., Souriot, T., Boccaletti, M., Brun, J.-P. 1997. Successive orthogonal and oblique extension episodes in a rift zone: Laboratory experiments with application to the Ethiopian Rift. *Tectonics* 16 (2), 347-362.
<https://doi.org/10.1029/96TC03935>
- Boutelier, D., Oncken, O. 2011. 3-D thermo-mechanical laboratory modeling of plate-tectonics: modeling scheme, technique and first experiments. *Solid Earth* 2, 35-51.
<https://doi.org/10.5194/se-2-35-2011>
- Buck, W.R. 1991. Models of Continental Lithospheric Extension. *Journal of Geophysical Research* 96, 20,161-20,178.
<https://doi.org/10.1029/91JB01485>
- Buiter, S.J.H., Huismans, R.S., Beaumont, C. 2008. Dissipation analysis as a guide to mode selection during crustal extension and implications for the styles of sedimentary basins. *Journal of Geophysical Research* 113, B06406.
<https://doi.org/10.1029/2007JB005272>
- Bürgman, R., Dresen, G., 2008. Rheology of the Lower Crust and Upper Mantle: Evidence from Rock Mechanics, Geodesy, and Field Observations. *Annual Review of Earth and Planetary Sciences* 36, 531-67.
<https://doi.org/10.1146/annurev.earth.36.031207.124326>
- Burov, E., Cloetingh, S. 1997. Erosion and rift dynamics: new thermomechanical aspects of post-rift evolution of extensional basins. *Earth and Planetary Science Letters* 150, 7-26.
[https://doi.org/10.1016/S0012-821X\(97\)00069-1](https://doi.org/10.1016/S0012-821X(97)00069-1)
- Burov, E., Guillou-Frottier, L., d'Acremont, E., Le Pourhiet, L., Cloetingh, S. 2007. Plume head–lithosphere interactions near intra-continental plate boundaries. *Tectonophysics* 434, 15-38.
<https://doi.org/10.1016/j.tecto.2007.01.002>
- Burov, E. 2011. Rheology and strength of the lithosphere. *Marine and Petroleum Geology* 28, 1403-1443.
<https://doi.org/10.1016/j.marpetgeo.2011.05.008>

- Brun, J.-P. 1999. Narrow rifts versus wide rifts: inferences for the mechanics of rifting from laboratory experiments. *Philosophical Transactions of the Royal Society London A* 357, 695-712.
<https://doi.org/10.1098/rsta.1999.0349>
- Brun, J.-P., Tron, V. 1993. Development of the North Viking Graben: inferences from laboratory modelling. *Sedimentary Geology* 86, 31-51.
[https://doi.org/10.1016/0037-0738\(93\)90132-O](https://doi.org/10.1016/0037-0738(93)90132-O)
- Brun, J.-P., Nalpas, T. 1996. Graben inversion in nature and experiments. *Tectonics* 15, 677-687.
<https://doi.org/10.1029/95TC03853>
- Cagnard, F., Brun, J.-P., Gapais, D. 2006. Modes of thickening of analogue weak lithospheres. *Tectonophysics* 421, 145-160. <https://10.1016/j.tecto.2006.04.016>
- Calignano, E., Sokoutis, D., Willingshofer, E., Gueydan, F., Cloetingh, S. 2015. Asymmetric vs. symmetric deep lithospheric architecture of intra-plate continental orogens. *Earth and Planetary Science Letters* 424, 38–50.
<http://dx.doi.org/10.1016/j.epsl.2015.05.022>
- Carlo AG (Carlo Bernasconi AG, Switzerland) 2018.
 Company website: www.carloag.ch
- Casas, A. M., D. Gapais, T. Nalpas, K. Besnard, and T. Román - Berdiel (2001), Analogue models of transpressive systems, *Journal of Structural Geology*, 23, 733–743,
[http://dx.doi.org/10.1016/S0191-8141\(00\)00153-X](http://dx.doi.org/10.1016/S0191-8141(00)00153-X)
- Chemenda, A., Déverchère, J., Calais, E. 2002. Three-dimensional laboratory modelling of rifting: application to the Baikal Rift, Russia. *Tectonophysics* 356, 253-273.
[https://doi.org/10.1016/S0040-1951\(02\)00389-X](https://doi.org/10.1016/S0040-1951(02)00389-X)
- Chorowicz, J., Collet, B., Bonavia, F., Korme, T. 1999. Left-lateral strike-slip tectonics and gravity induced individualisation of wide continental blocks in the western Afar margin. *Eclogae geologicae Helveticae* 92, 149–158.
<https://www.e-periodica.ch/cntmng?pid=egh-001:1999:92::596>
- Clifton, A.E., Schlische, R.W. 2001. Nucleation, growth and linkage of faults in oblique rift zones: Results from experimental clay models and implications for maximum fault size. *Geology* 29 (5), 455-458.
[https://doi.org/10.1130/0091-7613\(2001\)029<0455:NGALOF>2.0.CO;2](https://doi.org/10.1130/0091-7613(2001)029<0455:NGALOF>2.0.CO;2)
- Cobbold, P.R., Quinquis, H., 1980. Development of sheath folds in shear regimes. *Journal of Structural Geology* 2, 119–126.
- Colletta, B., Letouzey, J., Pinedo, R., Ballard, J.F., Balé, P. 1991. Computerized X-ray tomography analysis of sandbox models: Examples of thin-skinned thrust systems. *Geology* 19, 1063-1067.
[https://doi.org/10.1130/0091-7613\(1991\)019<1063:CXRTAO>2.3.CO;2](https://doi.org/10.1130/0091-7613(1991)019<1063:CXRTAO>2.3.CO;2)
- Corti, G. 2009. Continental rift evolution: From rift initiation to incipient break-up in the Main Ethiopian Rift, East Africa. *Earth-Science Reviews* 96, 1-53.
<https://doi.org/10.1016/j.earscirev.2009.06.005>

- Corti, G., Bonini, B., Conticelli, S., Innocenti, F., Manetti P., Sokoutis, D. 2003. Analogue modelling of continental extension: a review focused on the relations between the patterns of deformation and the presence of magma.
[https://doi.org/10.1016/S0012-8252\(03\)00035-7](https://doi.org/10.1016/S0012-8252(03)00035-7)
- Corti, G., Van Wijk, J., Cloetingh, S., Morley, C.K. 2007. Tectonic inheritance and continental rift architecture: Numerical and analogue models of the East African Rift system. *Tectonics* 26, TC6006.
<https://doi.org/10.1029/2006TC002086>
- Corti, G., Agostini, A., Keir, d., Van Wijk, J., Bastow, I.D., Ranalli, G. 2015. Magma-induced axial subsidence during final-stage rifting: Implications for the development of seaward-dipping reflectors. *Geosphere* 11 (3), 563-571.
<https://doi.org/10.1130/GES01076.1>
- Dauteuil, O., Brun, J.-P. 1993. Oblique rifting in a slow-spreading ridge. *Nature* 361, 145-148.
<https://doi.org/10.1038/361145a0>
- Dauteuil, O., Bourgeois, O., Mauduit, T. 2002. Lithosphere strength controls oceanic transform structure: insights from analogue models. *Geophysical Journal International* 150, 706-714.
[10.1046/j.1365-246X.2002.01736.x](https://doi.org/10.1046/j.1365-246X.2002.01736.x)
- Dixon, J.M., Summers, J.M., 1985. Recent developments in centrifuge modelling of tectonic processes: equipment, model construction techniques and rheology of model materials. *J. Struct. Geol.* 7, 83–102.
- Dooley, T.P., Schreurs, G. 2012. Analogue modelling of intraplate strike-slip tectonics: A review and new experimental results. *Tectonophysics* 574-575, 1-71.
<http://dx.doi.org/10.1016/j.tecto.2012.05.030>
- Eisenstadt, G., Sims, D. 2005. Evaluating sand and clay models: do rheological differences matter? *Journal of Structural Geology* 27, 1399–1412.
<https://doi.org/10.1016/j.jsg.2005.04.010>
- Elmohandes, S.-E. 1981. The Central European Graben System: Rifting Imitated by Clay Modelling. *Tectonophysics* 73, 69-78.
[https://doi.org/10.1016/0040-1951\(81\)90174-8](https://doi.org/10.1016/0040-1951(81)90174-8)
- Fadaie, K., Ranalli, G. 1990. Rheology of the lithosphere in the East African Rift System. *Geophysical Journal International* 102, 445-453.
<https://doi.org/10.1111/j.1365-246X.1990.tb04476.x>
- Fort, X., Brun, J.-P., Chauvel F. 2004. Salt tectonics on the Angolan margin, synsedimentary deformation processes. *AAPG Bulletin* 88 (11), 1523-1544.
<https://doi.org/10.1306/06010403012>
- Gartrell, A.P. 1997. Evolution of rift basins and low-angle detachments in multilayer analog models. *Geology* 25 (7), 615-618.
[https://doi.org/10.1130/0091-7613\(1997\)025<0615:EORBAL>2.3.CO;2](https://doi.org/10.1130/0091-7613(1997)025<0615:EORBAL>2.3.CO;2)
- Handin, J., 1969. On the Coulomb–Mohr failure criterion. *Journal of Geophysical Research* 74, 5343–5348.
<https://doi.org/10.1029/JB074i022p05343>
- Henza, A.A., Withjack, M.O., Schlische, R.W. 2010. Normal-fault development during two phases of non-coaxial extension: An experimental study. *Journal of Structural Geology* 32, 1656-1667.

1157 <https://doi.org/10.1016/j.jsg.2009.07.007>
1158
1159 Hirth, G. and D.L. Kohlstedt (2003), Rheology of the upper mantle and the mantle wedge: A
1160 view from the experimentalists. In: Eiler, J. (ed), Inside the Subduction Factory. American
1161 Geophysical Union Geophysical Monograph 138, 83-105.
1162 <https://doi.org/10.1029/138GM06>
1163
1164 Hubbert, M.K. 1937. Theory of scaled models as applied to the study of geological structures.
1165 Geological Society of America Bulletin 48, 1459-1520.
1166 <https://doi.org/10.1130/GSAB-48-1459>
1167
1168 Hubbert, M.K., 1951. Mechanical basis for certain familiar geological structures.
1169 Geological Society of America Bulletin 62, 355-372.
1170 [https://doi.org/10.1130/0016-7606\(1951\)62\[355:MBFCFG\]2.0.CO;2](https://doi.org/10.1130/0016-7606(1951)62[355:MBFCFG]2.0.CO;2)
1171
1172 Jaeger, J.C., Cook, N.G.W., 1976. Fundamentals of Rock Mechanics. Chapman & Hall, Wiley,
1173 New York.
1174
1175 Keep, M., McClay, K.R. 1997. Analogue modelling of multiphase rift systems. Tectonophysics
1176 273, 239
1177 [https://doi.org/10.1016/S0040-1951\(96\)00272-7](https://doi.org/10.1016/S0040-1951(96)00272-7)
1178
1179 Klinkmüller, M., Schreurs, G., Rosenau, M., Kemnitz, H. 2016. Properties of granular analogue
1180 model materials: A community wide survey. Tectonophysics 684, 23-38.
1181 <http://dx.doi.org/10.1016/j.tecto.2016.01.017>
1182
1183 Konstantinovskaya, E.A., Harris, L.B., Poulin, J., Ivanov, G.M. 2007. Transfer zones and fault
1184 reactivation in inverted rift basins: Insights from physical modelling. Tectonophysics 441, 1-26.
1185 <https://10.1016/j.tecto.2007.06.002>
1186
1187 Kranzt, R.W., 1991. Measurements of friction coefficients and cohesion for faulting and fault
1188 reactivation in laboratory models using sand and sand mixtures. Tectonophysics 188, 203-207.
1189 [https://doi.org/10.1016/0040-1951\(91\)90323-K](https://doi.org/10.1016/0040-1951(91)90323-K)
1190
1191 Le Calvez, J.H., Vendeville, B.C. 2002. Experimental designs to model along-strike fault
1192 interaction. Journal of the Virtual Explorer 7, 1-17.
1193 <https://doi.org/10.3809/jvirtex.2002.00043>
1194
1195 Mart, Y., Dauteuil, O. 2000. Analogue experiments of propagation of oblique rifts.
1196 Tectonophysics 316, 121-132.
1197 [https://doi.org/10.1016/S0040-1951\(99\)00231-0](https://doi.org/10.1016/S0040-1951(99)00231-0)
1198
1199 Marques, F.O. 2012. Transform faults orthogonal to rifts: Insights from fully gravitational
1200 physical models. Tectonophysics 526-529, 42-47.
1201 <https://doi.org/10.1016/j.tecto.2011.08.018>
1202
1203 McClay, K.R., White, M.J. 1995. Analogue modelling of orthogonal and oblique rifting. Marine
1204 and Petroleum Geology 12 (2), 137-151.
1205 [https://doi.org/10.1016/0264-8172\(95\)92835-K](https://doi.org/10.1016/0264-8172(95)92835-K)
1206
1207 McClay, K.R., Dooley, T., Whitehouse, P., Mills, M. 2002. 4-D evolution of rift systems: Insights
1208 from scaled physical models. AAPG Bulletin 86, 935-959.
1209 <http://www.searchanddiscovery.com/documents/mcclay03/images/mcclay03.pdf>
1210
1211 Michon, L., Merle, O. 2000. Crustal structures of the Rhinegraben and the Massif Central
1212 grabens: An experimental approach. Tectonics 19 (5), 896-904.
1213 <https://doi.org/10.1029/2000TC900015>

- Michon, L., Merle, O. 2003. Mode of lithospheric extension: Conceptual models from analogue modeling. *Tectonics* 22, 1028.
<https://doi.org/10.1029/2002TC001435>
- Montanari, D., Agostini, A., Bonini, M., Corti, G., Del Ventisette, C. 2017. The Use of Empirical Methods for Testing Granular Materials in Analogue Modelling. *Materials* 10, 635
<https://dx.doi.org/10.3390%2Fma10060635>
- Molnar, N.E., Cruden, A.R., Betts, P.G. 2017. Interactions between propagating rotational rifts and linear rheological heterogeneities: Insights from three-dimensional laboratory experiments. *Tectonics* 36, 420-443.
<https://doi.org/10.1002/2016TC004447>
- Mulugeta, G. 1988. Squeeze box in the centrifuge. *Tectonophysics* 148, 323-335.
[https://doi.org/10.1016/0040-1951\(88\)90139-4](https://doi.org/10.1016/0040-1951(88)90139-4)
- Naliboff, J., Buiter, S.J.H. 2015. Rift reactivation and migration during multiphase extension. *Earth and Planetary Science Letters* 421, 58–67.
<http://dx.doi.org/10.1016/j.epsl.2015.03.050>
- Nalpas, T., Brun, J.-P. 1993. Salt flow and diapirism related to extension at crustal scale. *Tectonophysics* 228, 349-362.
[https://doi.org/10.1016/0040-1951\(93\)90348-N](https://doi.org/10.1016/0040-1951(93)90348-N)
- Panien, M., Schreurs, G., Pfiffner, A. 2005. Sandbox experiments on basin inversion: testing the influence of basin orientation and basin fill. *Journal of Structural Geology* 27, 433-445.
<https://doi.org/10.1016/j.jsg.2004.11.001>
- Panien, M., Schreurs, G., Pfiffner, A. 2006. Mechanical behaviour of granular materials used in analogue modelling: insights from grain characterisation, ring-shear tests and analogue experiments. *Journal of Structural Geology* 28, 1710-1724.
<https://doi.org/10.1016/j.jsg.2006.05.004>
- Philippon, M., Willingshofer, E., Sokoutis, D., Corti, G., Sani, F., Bonini, M., Cloetingh, S. 2015. Slip re-orientation in oblique rifts. *Geology* 43, 147-150.
<https://doi.org/10.1130/G36208.1>
- Ramberg, H. 1981. *Gravity, Deformation and the Earth's Crust*. Academic Press, London.
- Román-Berdiel, T., Aranguren, A., Cuevas, J., Tubía, J.M., Gaipas, D., Brun, J.-P. 2000. Experiments on granite intrusion in transtension. In: Vendeville, B., Mart, Y., Vigneresse, J.-L. (eds) *Salt, Shale and Igneous Diapirs in and around Europe*. Geological Society, London, Special Publications 174, 21-42.
<https://doi.org/10.1144/GSL.SP.1999.174.01.02>
- Rudolf, M., Boutelier, D., Rosenau, M., Schreurs, G., Oncken, O. 2015. Rheological benchmark of silicone oils used for analog modeling of short- and long-term lithospheric deformation. *Tectonophysics* 684, 12-22.
<http://dx.doi.org/10.1016/j.tecto.2015.11.028>
- Rybacki, E., Gottschalk, M., Wirth, R., Dresen, G. (2006), Influence of water fugacity and activation volume on the flow properties of fine-grained anorthite aggregates. *Journal of Geophysical Research* 111 (B3)
<https://doi.org/10.1029/2005JB003663>

- Saria, E., Calais, E., Stamps, D.S., Delvaux, D., Hartnady, C.J.H. 2014. Present-day kinematics of the East African Rift. *Journal of Geophysical Research. Solid Earth* 119, 3584-3600.
<https://doi.org/10.1002/2013JB010901>
- Saunders, A.D., Storey, M., Kent, R.W., Norry, M.J. 1992. Consequences of plume-lithosphere interactions. Geological Society, London, Special Publications 68, 41-60.
<https://doi.org/10.1144/GSL.SP.1992.068.01.04>
- Schellart, W.P., Lister, G.S., Jessell, M.W. 2002. Analogue modelling of asymmetrical back-arc extension. In: Schellart, W.P., Passchier, C. (eds.) *Analogue modelling of large-scale tectonic processes*. *Journal of the Virtual Explorer* 7, 25-42.
<https://doi.org/10.3809/jvirtex.2002.00046>
- Schellart, W.P., Jessell, M.W., Lister, G.S. 2003. Asymmetric deformation in the backarc region of the Kuril arc, northwest Pacific: New insights from analogue modelling. *Tectonics*, 22 (5), 1047.
<https://doi.org/10.1029/2002TC001473>
- Schellart, W.P., Strak, V. 2016. A review of analogue modelling of geodynamic processes: Approaches, scaling, materials and quantification, with an application to subduction experiments. *Journal of Geodynamics* 100, 7-32.
<https://doi.org/10.1016/j.jog.2016.03.009>
- Schlagenhauf, A., Manighetti, I., Malavieille, J., Dominguez, S., 2008. Incremental growth of normal faults: Insights from a laser-equipped analog experiment. *Earth and Planetary Science Letters* 273, 299–311
<https://doi.org/10.1016/j.epsl.2008.06.042>
- Schreurs, G., Colletta, B. 1998. Analogue modelling of faulting in zones of continental transpression and transtension. Geological Society, London, Special Publications, 135, 59-79.
<https://doi.org/10.1144/GSL.SP.1998.135.01.05>
- Schreurs, G., Buiter, S.J.H., Boutelier, D., Corti, G., Costa, E., Cruden, A.R., Daniel, J.-M., Hoth, S., Koyi, H.A., Kukowski, N., Lohrmann, J., Ravaglia, A., Schlische, R.W., Withjack, M.O., Yamada, Y., Cavozi, C., Delventisette, C., Brady, J.A.E., Hoffmann-Rothe, A., Mengus, J.-M., Montanari, D., Nilforushan, F. 2006. Analogue benchmarks of shortening and extension experiments. In: Buiter, S.J.H., Schreurs, G. (eds.) *Analogue and Numerical Modelling of Crustal-Scale Processes*. Geological Society, London, Special Publications 253, 1-27.
<https://doi.org/10.1144/GSL.SP.2006.253.01.01>
- Schreurs, G., Buiter, S.J.H., Boutelier, J., Burberry, C., Callot, J.-P. Cavozi, C., Cerca, M., Chen, J.-H., Cristallini, E., Cruden, A.R., Cruz, L., Daniel, J.-M., Da Poian, G., Garcia, V.H., Gomes, C.J.S., Grall, C., Guillot, Y., Guzmán, C., Hidayah, T.N., Hilley, G., Klinkmüller, M., Koyi, H.A., Lu, C.-Y., Maillot, B., Meriaux, C., Nilfouroushan, F., Pan, C.-C., Pillot D., Portillo, R., Rosenau, M., Schellart, W.P., Schlische, R.W., Take, A., Vendeville, B., Vergnaud, M., Vettori, M., Wang, S.-H., Withjack, M.O., Yagupsky, D., Yamada, Y. 2016. Benchmarking analogue models of brittle thrust wedges. *Journal of Structural Geology* 92, 116-139.
<https://doi.org/10.1016/j.jsg.2016.03.005>
- Serra, S., Nelson, R.A. 1988. Clay modeling of rift asymmetry and associated structures. *Tectonophysics* 153, 307-312.
[https://doi.org/10.1016/0040-1951\(88\)90023-6](https://doi.org/10.1016/0040-1951(88)90023-6)
- Shinevar, W.J., Behn, M.D., Hirt, G., 2015. Compositional dependence of lower crustal viscosity. *Geophysical Research Letters* 42, 8333–8340.
<https://doi.org/10.1002/2015GL065459>

- Smith, J.V., Durney, D.W. Experimental formation of brittle structural assemblages in oblique divergence. *Tectonophysics* 216, 235-253.
[https://doi.org/10.1016/0040-1951\(92\)90399-Q](https://doi.org/10.1016/0040-1951(92)90399-Q)
- Sun., Z., Zhong, Z., Keep, M., Zhou, D., Cai, D., Li, X., Wu, S., Jiang, J. 2009. 3D analogue modelling of the South China Sea: A discussion on breakup pattern. *Journal of Asian Earth Sciences* 34, 544-556.
<https://doi.org/10.1016/j.jseaes.2008.09.002>
- Tetreault, J.L., Buiter, S.J.H. 2017. The influence of extension rate and crustal rheology on the evolution of passive margins from rifting to break-up
<https://doi.org/10.1016/j.tecto.2017.08.029>
- Tron, V. Brun, J.-P. 1991, Experiments on oblique rifting in brittle-ductile systems. *Tectonophysics* 188, 71-88.
[https://doi.org/10.1016/0040-1951\(91\)90315-J](https://doi.org/10.1016/0040-1951(91)90315-J)
- Twiss, R.J., Moores, E.M., 1992. *Structural Geology*. W.H. Freeman and Company, New York
- Ustaszewski, K., Schumacher, M.E., Schmid, S.M., Nieuwland, D. 2005. Fault reactivation in brittle–viscous wrench systems—dynamically scaled analogue models and application to the Rhine–Bresse transfer zone. *Quaternary Science Reviews* 24, 365-382.
<https://doi.org/10.1016/j.quascirev.2004.03.015>
- Vendeville, B., Cobbold, P.R., Davy, P., Brun, J.-P., Choukroune, P. 1987. Physical models of extensional tectonics at various scales. In: Coward, M.P., Dewey, J.F., Hancock, P.L. (eds.) *Continental Extensional Tectonics*. Geological Society, London, Special Publications 28, 95-107.
<https://doi.org/10.1144/GSL.SP.1987.028.01.08>
- Venkat-Ramani, M., Tikoff, B. 2002. Physical models of transtensional folding. *Geology* 30, 523-526.
[https://doi.org/10.1130/0091-7613\(2002\)030<0523:PMOTF>2.0.CO;2](https://doi.org/10.1130/0091-7613(2002)030<0523:PMOTF>2.0.CO;2)
- Weijermars, R. 1986. Flow behaviour and physical chemistry of bouncing putties and related polymers in view of tectonic laboratory applications. *Tectonophysics* 124, 325-358. [https://doi.org/10.1016/0040-1951\(86\)90208-8](https://doi.org/10.1016/0040-1951(86)90208-8)
- Weijermars, R., Schmeling, H. 1986. Scaling of Newtonian and non-Newtonian fluid dynamics without inertia for quantitative modelling of rock flow due to gravity (including the concept of rheological similarity). *Physics of Earth and Planetary Interiors* 43, 316-330.
[https://doi.org/10.1016/0031-9201\(86\)90021-X](https://doi.org/10.1016/0031-9201(86)90021-X)
- Xia, Q.K., Hao, Y.T. 2010. The distribution of water in the continental lithospheric mantle and its implications for the stability of continents. *Chinese Science Bulletin* 58, 3897-3889.
<https://doi.org/10.1007/s11434-013-5949-1>
- Zulauf, J., Zulauf, G. 2004. Rheology of plasticine used as rock analogue: the impact of temperature, composition and strain. *Journal of Structural Geology* 26, 725–737.
<https://doi.org/10.1016/j.jsg.2003.07.005>
- Zwaan, F., G. Schreurs, J. Naliboff, Buiter, S.J.H. 2016. Insights into the effects of oblique extension on continental rift interaction from 3D analogue and numerical models. *Tectonophysics* 693, 239-260.
<https://doi.org/10.1016/j.tecto.2016.02.036>

1384 Zwaan, F., Schreurs, G. 2017. How oblique extension and structural inheritance influence rift
1385 segment interaction: Insights from 4D analog models. Interpretation 5 (1), SD119-SD138.
1386 <https://doi.org/10.1190/INT-2016-0063.1>
1387
1388 Zwaan, F., Schreurs, G. Adam, J., 2017. Effects of sedimentation on rift segment evolution and
1389 rift interaction in orthogonal and oblique extensional settings: Insights from analogue models
1390 analysed with 4D X-ray computed tomography and digital volume correlation techniques.
1391 Global and Planetary Change.
1392 <https://doi.org/10.1016/j.gloplacha.2017.11.002>
1393
1394
1395
1396
1397
1398
1399
1400
1401

Table captions

Table 1. Material properties

Granular materials	Quartz sand ^a	Corundum sand ^b
Grain size range	60-250 μm	88-175 μm
Density (specific) ^c	2650 kg/m^3	3950 kg/m^3
Density (sieved)	1560 kg/m^3	1890 kg/m^3
Angle of internal peak friction	36.1°	37°
Angle of dynamic-stable friction	31.4°	32°
Cohesion	9 \pm 98 Pa	39 \pm 10 Pa
Viscous material	PDMS/corundum sand mixture ^a	
Pure PDMS density (specific) ^a	0.965 kg/m^3	
Weight ratio PDMS : corundum sand	0.965 kg : 1.00 kg	
Mixture density	ca. 1600 kg/m^3	
Viscosity ^d	ca. $1.5 \cdot 10^5 \text{ Pa}\cdot\text{s}$	
Type	near-Newtonian ($n = 1.05$) ^e	

^a Quartz sand, pure PDMS and viscous mixture characteristics after Zwaan et al. (2016)

^b Corundum sand characteristics after Panien et al. (2006)

^c Specific densities of quartz and corundum sands after Carlo AG (2018)

^d The viscosity value holds for model strain rates $< 10^{-4} \text{ s}^{-1}$

^e Stress exponent n (dimensionless) represents sensitivity to strain rate

1415 Table 2. List of models
1416

	Model	Layering		Seed	Extension		Shown in:
		Type	Thickness (brittle/ viscous)		Type	Velocity	
Foam base (F series)	F1	Brittle only	40/- mm	No	Symmetric	8 mm/h	Fig. 4
	F2			8 mm/h			
	F3			8 mm/h			
	F4 ^{CT}			8 mm/h		Fig. 4	
	F5	Brittle-viscous	40/40 mm	No		8 mm/h	Fig. 5
	F6			8 mm/h			
	F7 ^{CT}			8 mm/h		Fig. 5	
Rubber base (R series)	R1 ^a	Brittle only	40/- mm	No seed	Symmetric	1 st phase: 8 mm/h 2 nd phase: 40 mm/h	Fig. 6
	R2 ^b			Seed		10 mm/h	
	R3 ^b					20 mm/h	
	R4 ^{CT, b}					20 mm/h	
	R5 ^{CT, b}					10 mm/h	Fig. 6
	R6 ^{CT, d}					20 mm/h	
	R7 ^a	Brittle-viscous	40/40 mm	No seed		1 st phase: 8 mm/h 2 nd phase: 40	Fig. 7
	R8			Seed		8 mm/h	Fig. 7
	R9			No seed		80 mm/h	Fig. 7
	R10			Seed		480 mm/h	Fig. 7
Plate base (P series)	P1	Brittle only	40/- mm	No seed	Symmetric	8 mm/h	Fig. 8
	P2				Asymmetric	8 mm/h	Fig. 8
	P3	Brittle-viscous	40/40 mm		Symmetric	8 mm/h	
	P4					2 mm/h	
	P5					40 mm/h	
	P6				8 mm/h		
	P7				Asymmetric	8 mm/h	Fig. 8
	P8 ^e		Symmetric		2 mm/h	Fig. 8	
	P9 ^e				80 mm/h	Fig. 8	
	P10			8 mm/h	Fig. 8		
Conveyor base (C series)	C1	Brittle only	40/- mm	No seed	Symmetric	40 mm/h	Fig. 9
	C2				Asymmetric	40 mm/h	
	C3					40 mm/h	Fig. 9
	C4	Brittle-viscous	40/40 mm		Symmetric	8 mm/h	Fig. 9
	C5 ^T					8 mm/h	
	C6 ^T					8 mm/h	
	C7		40/20 mm			8 mm/h	Fig. 9
	C8		40/10 mm			8 mm/h	Fig. 9
	C9					80 mm/h	
	C10					40 mm/h	
	C11 ^{CT}		20/20 mm			40 mm/h	Fig. 9
	C12 ^e					80 mm/h	

1417
1418 Bold Shown in this article
1419 CT CT-scanned models
1420 a Two-phase model with 40 mm of extension at 8 mm/h followed by 20 mm of extension at 40 mm/h
1421 b Initial model width 25 cm instead of 30 cm
1422 c 54 mm total extension; rubber sheet ripped partly after ca. 2 h (40 mm extension)
1423 d Total extension: 60 mm
1424 e Models with a total 40 mm thickness (20 mm brittle, 20 mm viscous) and 20 mm total extension
1425 f Attempt to reduce boundary effects (see text and Fig. B2 in Appendix B for details)
1426

1427 Table 3. Scaling parameters
1428

	General parameters			Brittle upper crust		Ductile lower crust		Dynamic scaling values	
	Gravitational acceleration g (m/s^2)	Upper crustal thickness h (m)	Extension velocity v (m/s)	Density ρ (kg/m^3)	Cohesion C (Pa)	Density ρ (kg/m^3)	Viscosity η (Pa·s)	Ramberg number R_m	Brittle stress ratio R_s
Model (reference)	9.81	$4 \cdot 10^{-2}$	$2.2 \cdot 10^{-6}$	1560	9	1600	$1.5 \cdot 10^5$	75	68
Nature	9.81	$2 \cdot 10^4$	$1.5 \cdot 10^{-10}$	2800	$8 \cdot 10^6$	2870	$1 \cdot 10^{21}$	75	68

1429
1430
1431

1432 Table 4. Overview of links between our analogue set-ups, the resulting structures observed in
 1433 our experiments and their natural analogues
 1434

Type	Layering	Extension velocity	Brittle-viscous ratio used	Coupling observed in experiments	Natural analogue	Structural style observed in experiments
Foam/Rubber	Brittle	Slow	-	Very high coupling of brittle layer with substratum	Strong ductile lower crust (Fig. 3a)	No seed: wide rifting (Fig. 10a, a')
						Seed: wide rifting with small localized graben (Fig. 10b, b')
						NB: Rubber base: conjugate faults may occur! (Fig. 10e, e', f, f')
	Brittle-viscous	Slow	1:1	Low coupling between all components*	Weak, hot lithosphere (strong mantle absent) (Fig. 3b)	No seed: only boundary effects (Fig. 10c, c')
			1:1	High coupling between all components	Strong ductile lower crust, but weak ductile upper mantle (Fig. 3e)	Seed: localized rifting (Fig. 10d, d')
		Fast	1:1	High coupling between all components	Strong ductile lower crust, but weak ductile upper mantle (Fig. 3e)	No seed: wide rifting (Fig. 10m, m')
Plate/Conveyor belt	Brittle	Slow	-	Very high coupling of brittle layer with substratum	Cold lithosphere; Fault in (thick) brittle crust or brittle mantle (Fig. 3c).	Seed: wide rifting with a localized graben (e.g. Zwaan et al. 2016)
						Narrow rifting (Fig. 10i, i', j, j')
	Brittle-viscous	Slow	1:1	Low coupling between all components*	Hot lithosphere with thick ductile lower crust above brittle upper mantle (Fig. 3d)	No seed: wide rifting (Fig. 10k, k)
			1:1	Low coupling between all components*	Hot lithosphere with thick ductile lower crust above brittle upper mantle (Fig. 3d)	Seed: wide rifting with small localized graben (Fig. 10l, l')
			4:1	High coupling between all components*	Cold lithosphere with thin ductile lower crust above brittle upper mantle (Fig. 3h)	No seed: Wide (double) rifting (Fig. 10o, o')
			4:1	High coupling between all components*	Cold lithosphere with thin ductile lower crust above brittle upper mantle (Fig. 3h)	Seed: Not known
		Fast	1:1	Very high coupling between all components*	Hot lithosphere with thick ductile lower crust above brittle upper mantle (Fig. 3f)	No seed: Downbending basin (Fig. 10m, m')
			1:1	Very high coupling between all components*	Hot lithosphere with thick ductile lower crust above brittle upper mantle (Fig. 3f)	Seed: Not known
			4:1	Very high coupling between all components*	Cold lithosphere with thin ductile lower crust above brittle upper mantle (Fig. 3h)	Narrow (double) rifting (Fig. 10p, p')
			4:1	Very high coupling between all components*	Cold lithosphere with thin ductile lower crust above brittle upper mantle (Fig. 3h)	Seed: Not known

1435
 1436 (*) all components: all parts of the set-up, i.e. the sand layer, viscous layer and
 1437 substratum (or base of the set-up)

Figures + captions

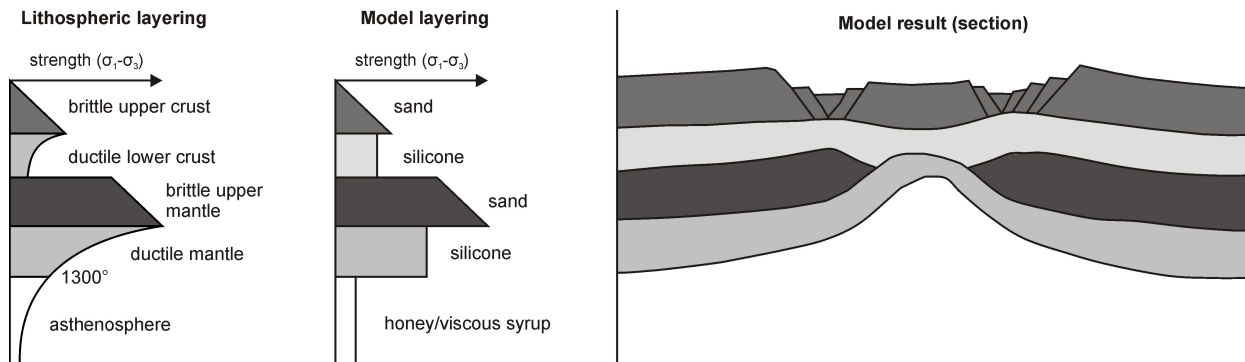


Fig. 1. Example of model layering to simulate extension in a stable four-layer lithosphere. Left: strength profile of the natural example, with a brittle upper crust, a ductile lower crust, a strong brittle upper mantle and a ductile lower mantle that blends into the underlying asthenosphere at a temperature of 1300°C . Middle: model materials representing the various layers: sand for the brittle parts of the lithosphere, viscous silicone (mixtures) for the ductile crust and mantle. The asthenosphere is simulated with a honey or viscous syrup. Right: cross-section at the end of the extension experiment. Adapted from Allemand & Brun (1991) with permission from Elsevier.

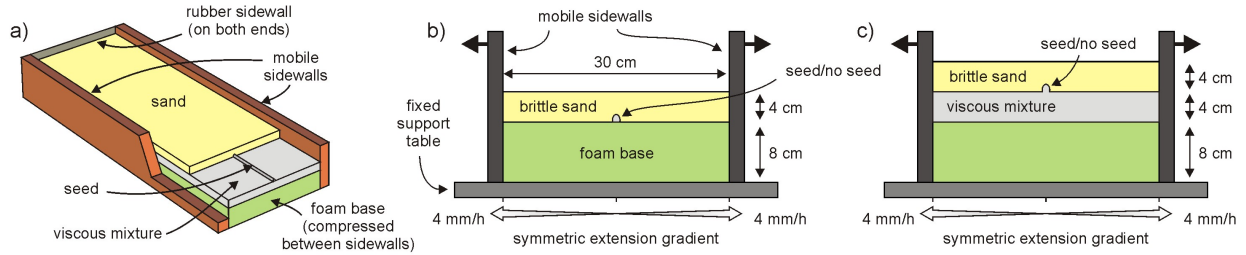
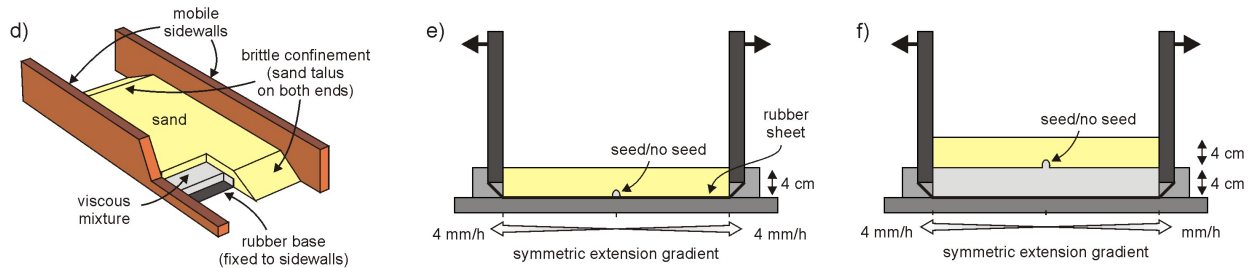
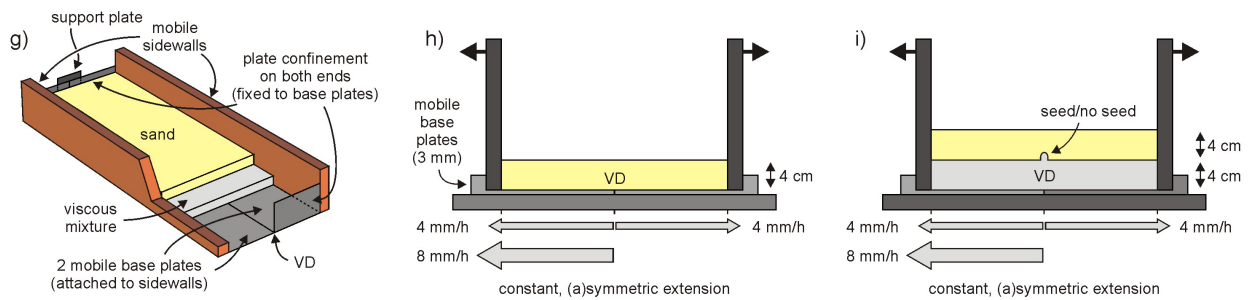
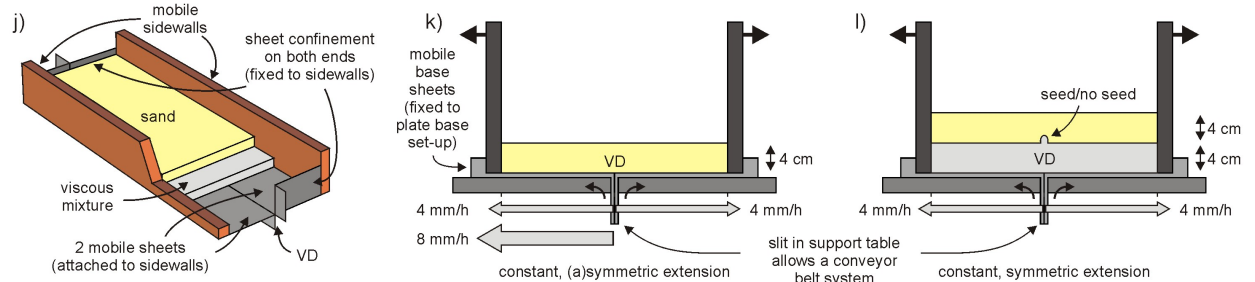
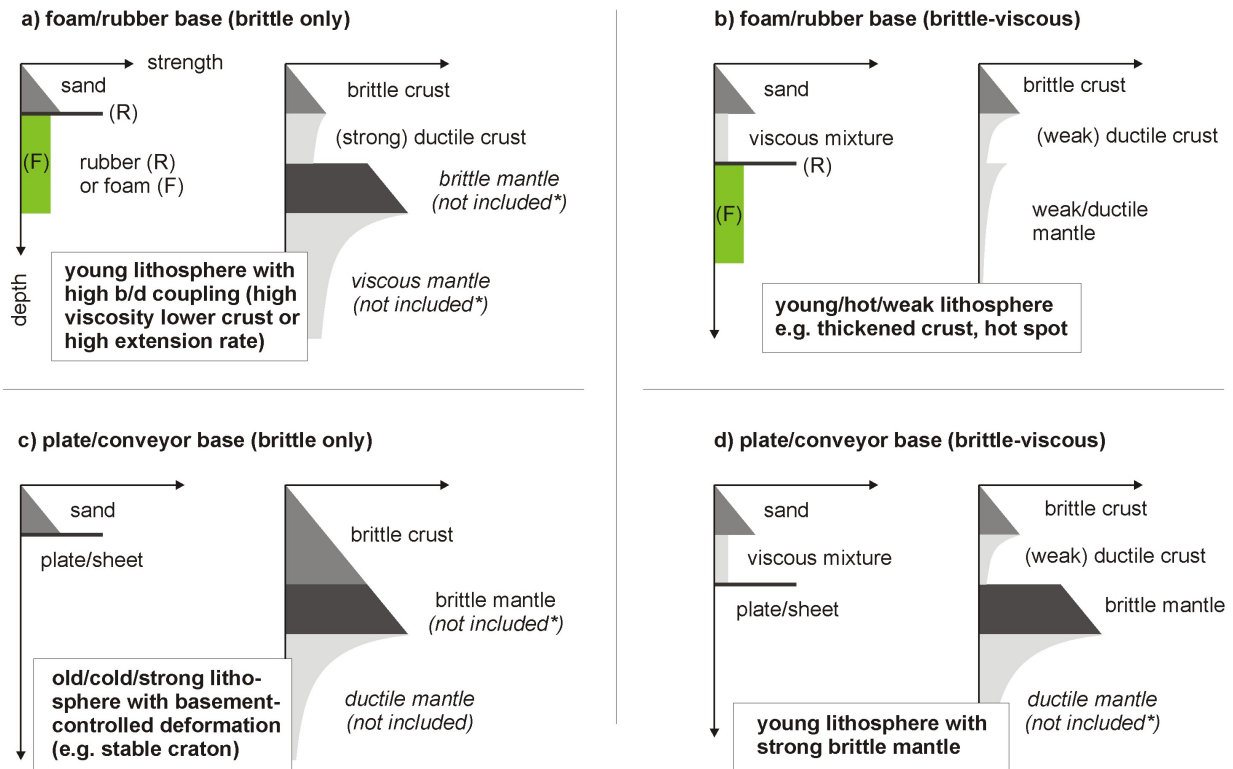
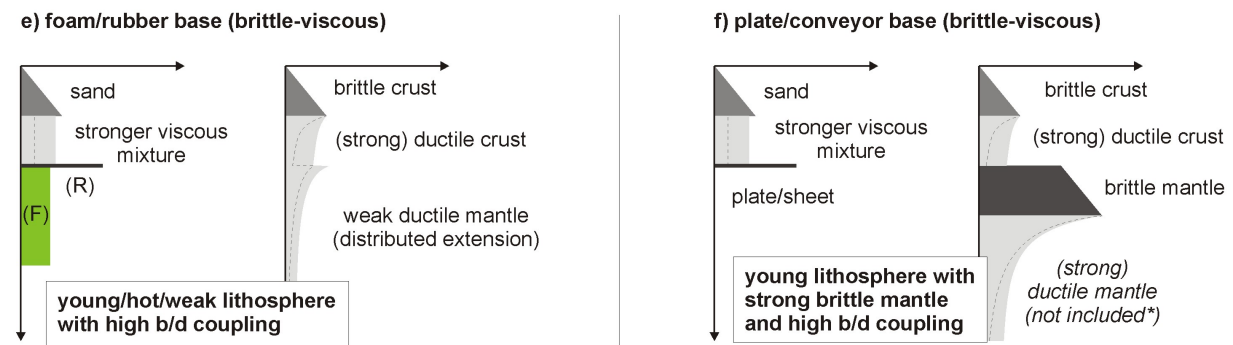
Foam base experiments (F series)**Rubber base experiments (R series)****Plate base experiments (P series)****Conveyor base experiments (C series)**

Fig. 2. Reference set-ups tested for this paper. See Table 2 for a complete overview of the specific model parameters applied in this study. Note that the 3D cut-out views show examples of reference set-ups with brittle-viscous layering. VD: velocity discontinuity. For details on the additional set-ups, see Table 2.

Reference experiments (reference parameters)



High velocity experiments



Viscous layer thickness variations

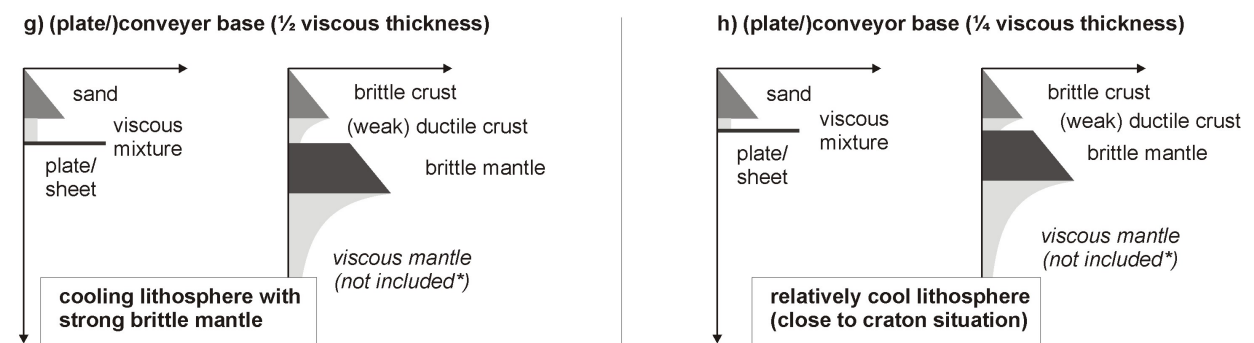


Fig. 3. Schematic experimental and natural strength profiles (always left and right, respectively), indicating the lithospheric setting that experiments may represent. Dotted lines in (e) and (f) indicate the strength profile under reference conditions for comparison. (*) the effects of these layers are not included in the set-up. b/d = brittle/ductile.

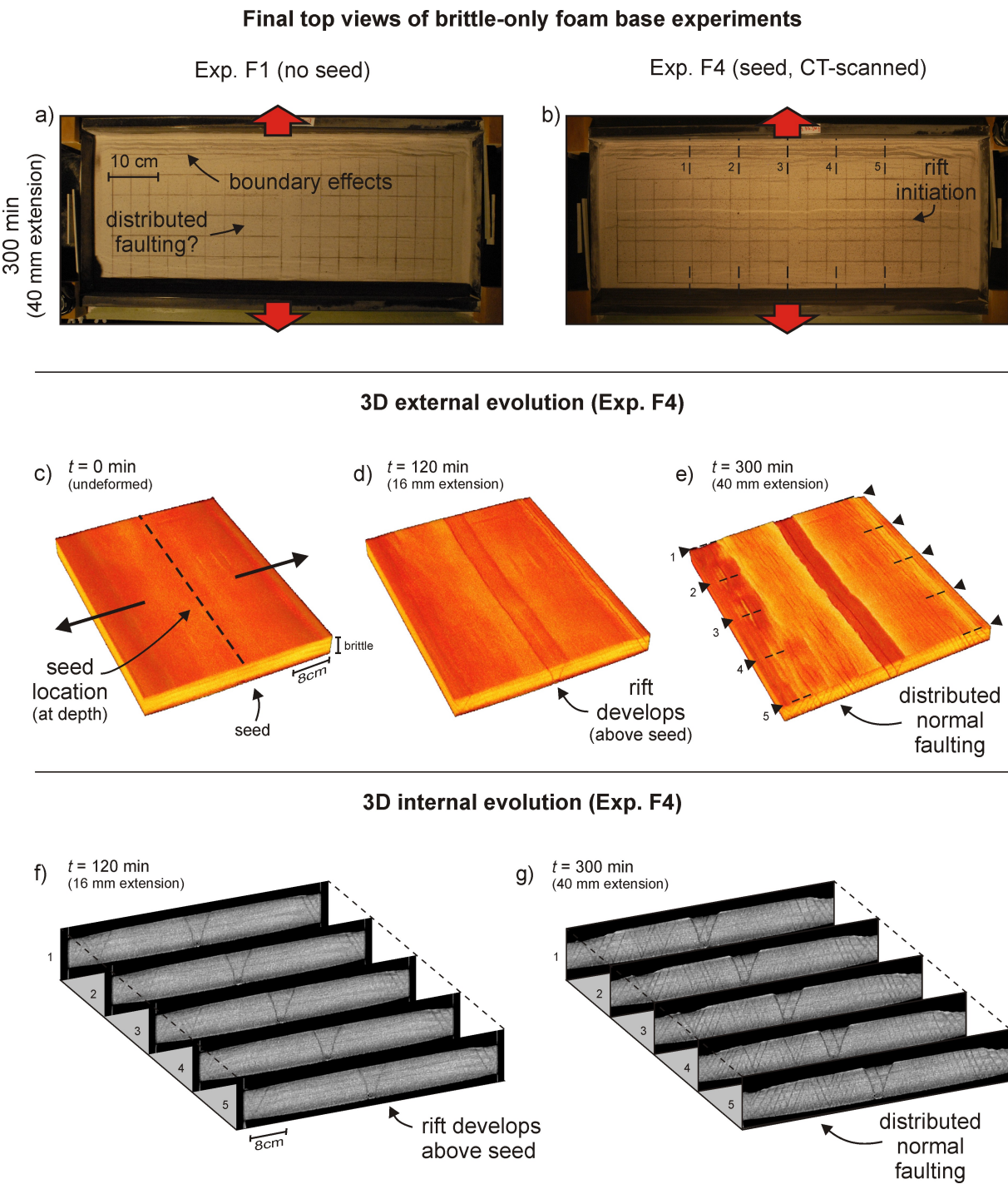
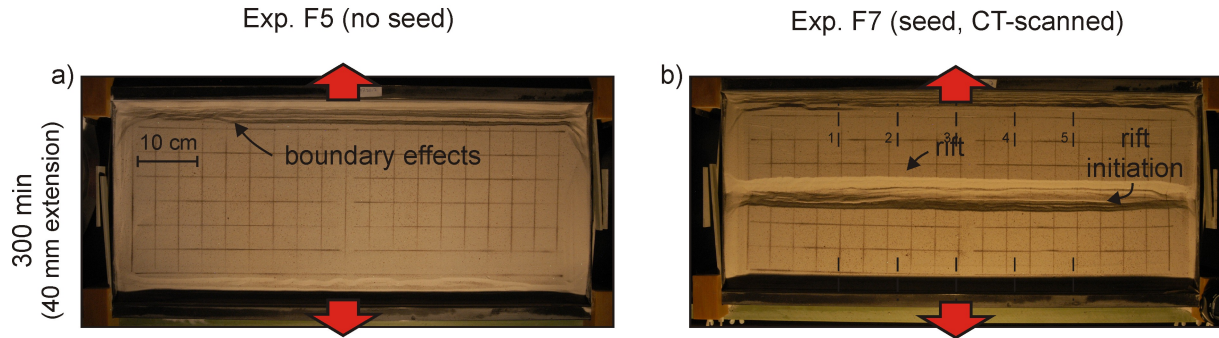
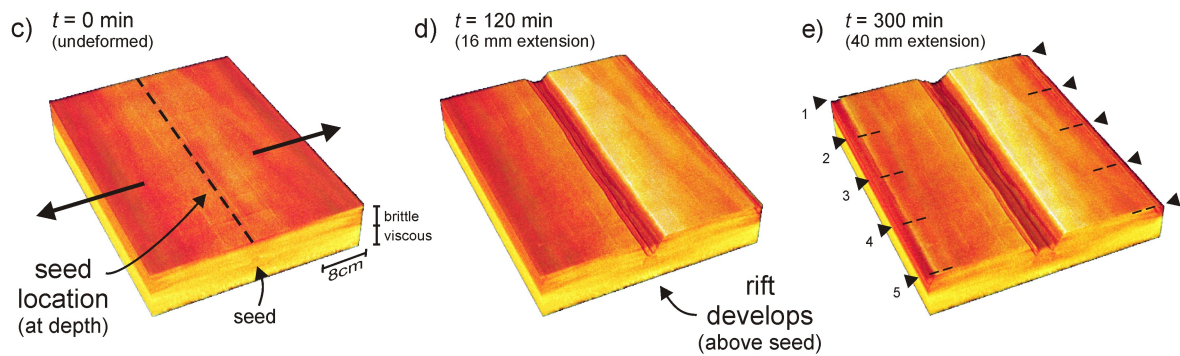


Fig. 4. Foam base (brittle-only) results. (a, b) Top views depicting the final surface structures of models F1 (no seed) and F4 (with seed). The brittle layer is 4 cm thick and the extension velocity is 8 mm/h. Note that the boundary effects are present on both sides of the model, but these are partially invisible due to shadow. (c-d) 3D evolution of CT-scanned model F4. (f, g) 3D internal evolution of CT-scanned model F4.

Final top views of brittle-viscous foam base experiments



3D external evolution (Exp. F7)



3D internal evolution (Exp. F7)

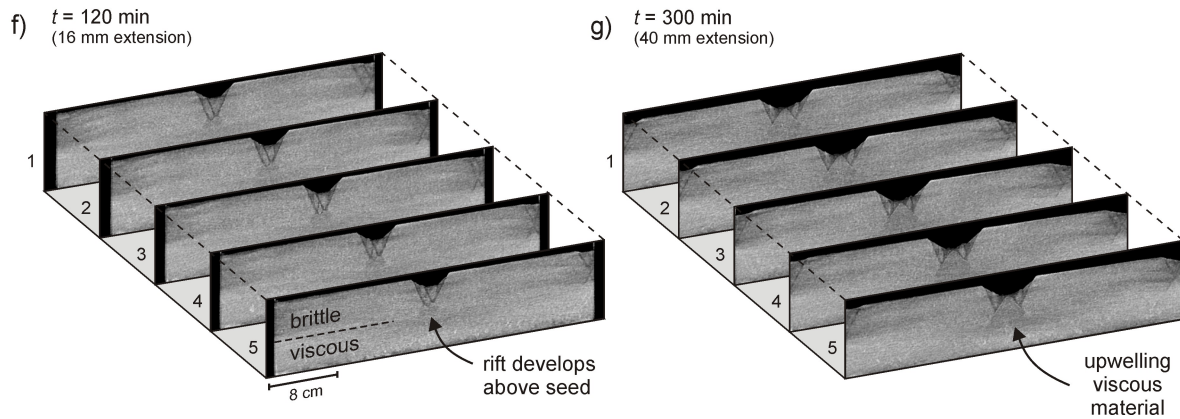
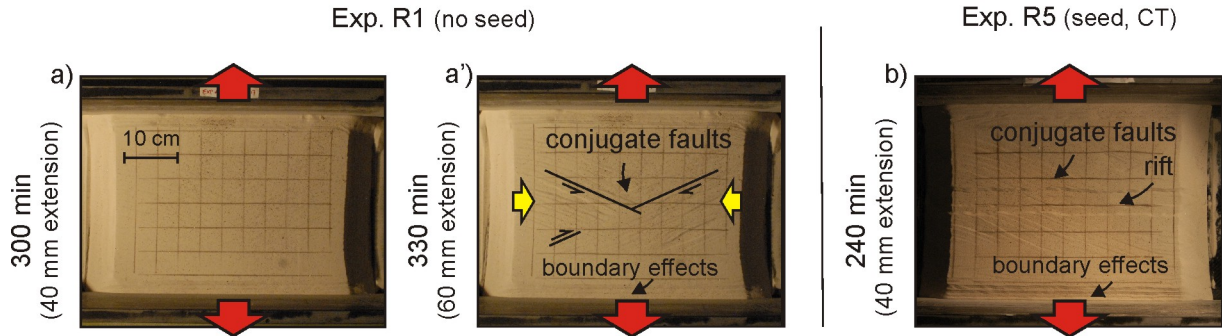
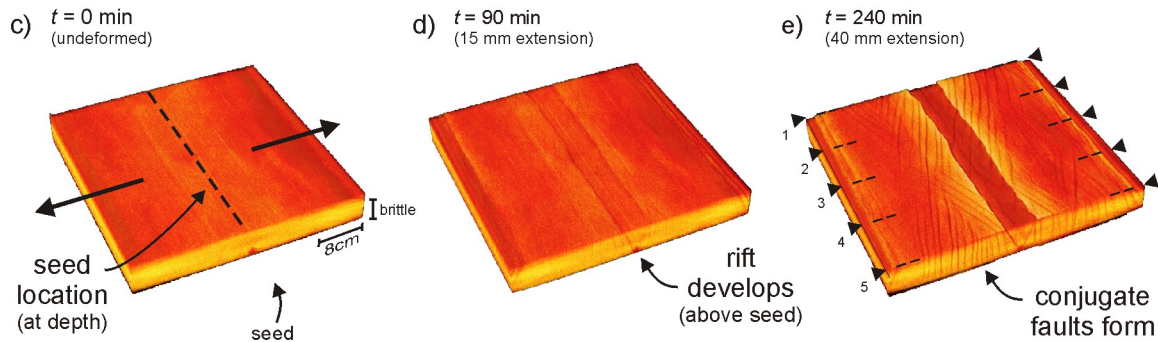


Fig. 5. Foam base (brittle-viscous) results. (a, b) Top views depicting the final surface structures of experiments F5 (no seed) and F7 (with seed). Both the brittle and viscous layers are 4 cm thick and the extension velocity is 8 mm/h. Note that the boundary effects are present on both sides of the model, but these are partially invisible due to shadow. (c-d) 3D evolution of CT-scanned model F7. (f, g) 3D internal evolution of CT-scanned model F7.

Final top views of brittle-only rubber base experiments



3D external evolution (Exp. R5)



3D internal evolution (Exp. R5)

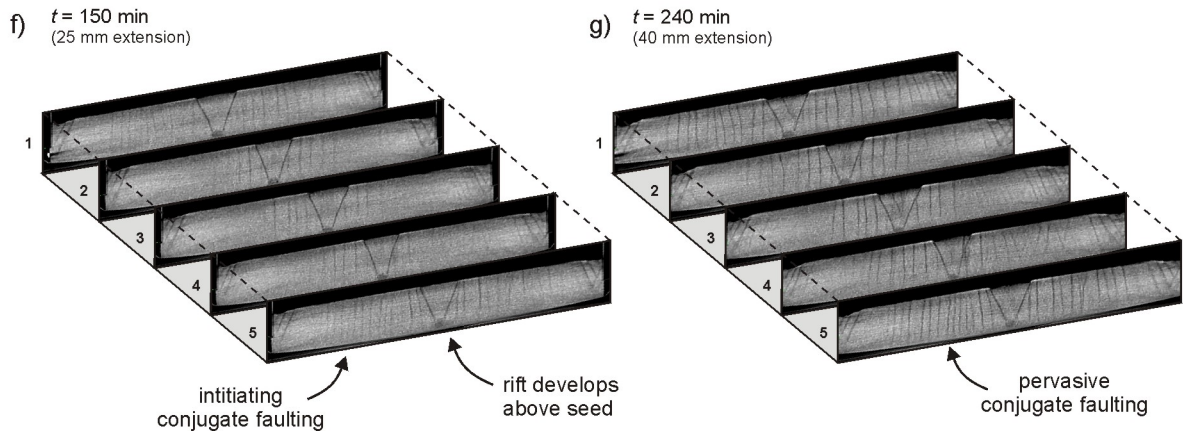
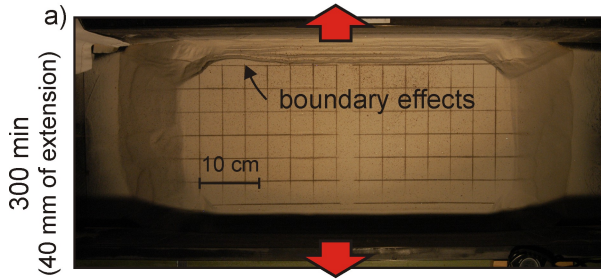


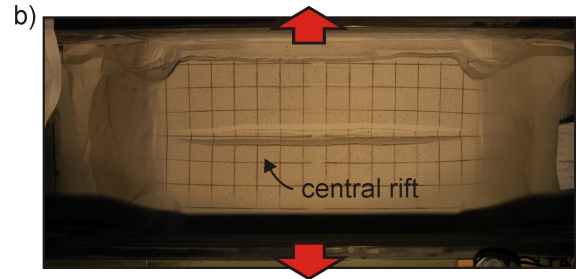
Fig. 6. Rubber base (brittle-only) results. (a, b) Top views depicting surface structures of experiments R1 (no seed) and R5 (with seed) after 40 mm of extension. Note that (a) represents the first phase of experiment R1 (8 mm/h), whereas and additional 20 mm of extension was applied with an enhanced extension velocity of 20 mm/h to amplify structures. Experiment R5 was run with an extension velocity of 10 mm/h. These deviations from the reference extension velocity (8 mm/h) are permissible, since the behaviour of sand is time-independent. The sand layer is 4 cm thick in both experiments. (c-d) 3D evolution of CT-scanned model R5. (f, g) 3D internal evolution of CT-scanned experiment R5. Note that the boundary effects are present on both sides of the model, but these are partially invisible due to shadow.

Final top views of brittle-viscous rubber base experiments

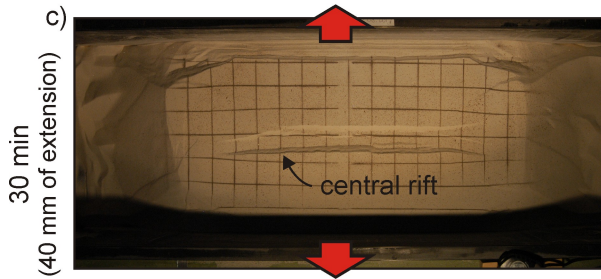
Exp. R7 (no seed, 8 mm/h)



Exp. R8 (seed, 8 mm/h)



Exp. R9 (no seed, 80 mm/h)



Exp. R10 (no seed, 480 mm/h)

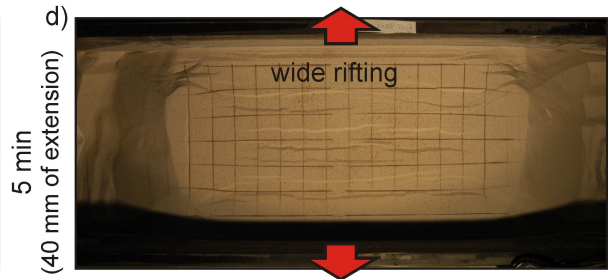
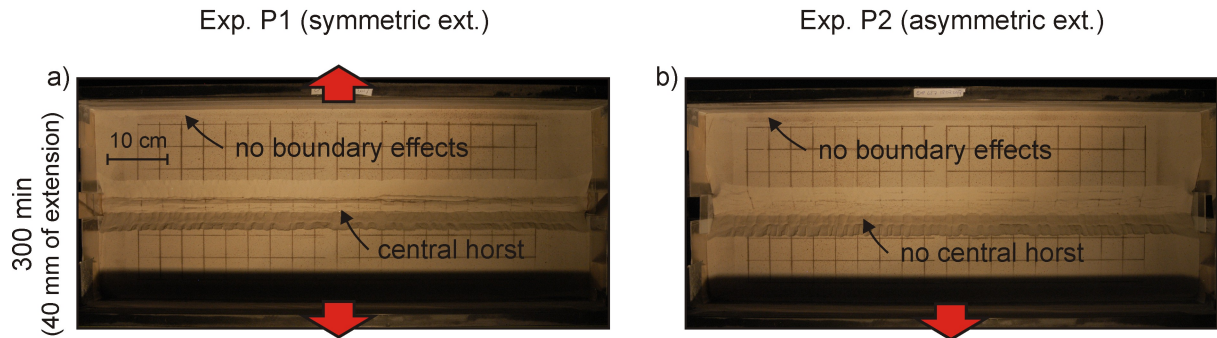


Fig. 7. Rubber base (brittle-viscous) results. Top views depicting the final surface structures of (a, b) experiments R7 and R8 (reference extension velocity of 8 mm/h) and (c, d) R9 and R10 (high extension velocity experiments: 80 and 480 mm/h, respectively). Note that boundary effects, although partially invisible due to shadow, are present on all sides of the model and therefore especially in the corners.

Final top views of brittle-only plate base experiments



Final top views of brittle-viscous plate base experiments

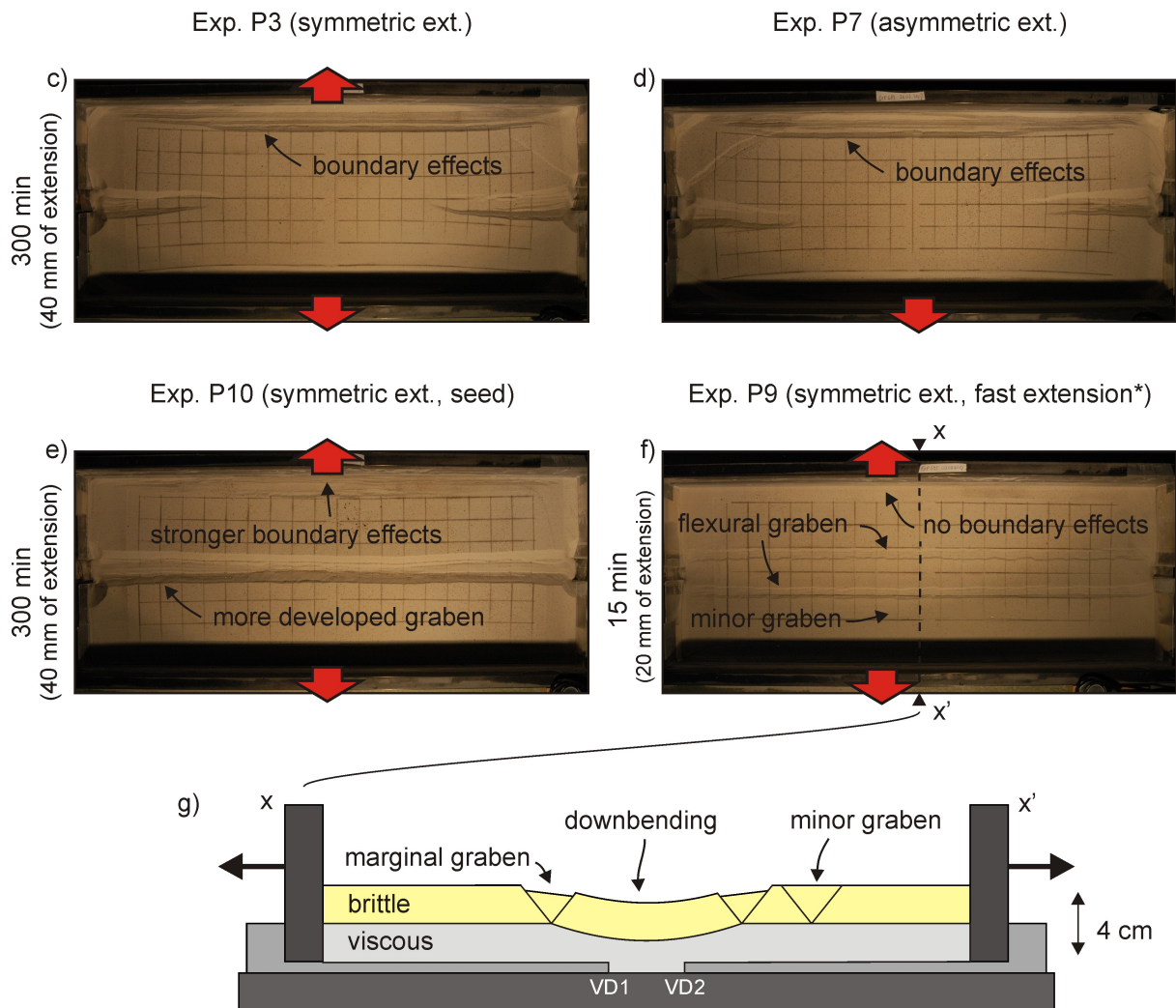
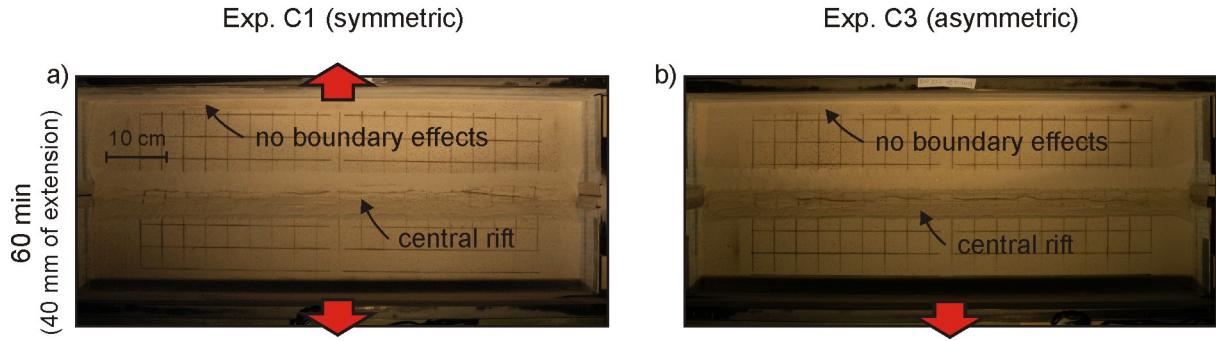


Fig. 8. Overview depicting our plate base results. (a, b) Top views of brittle-only experiments P1 (symmetric extension) and P2 (asymmetric extension). (c-f) Brittle-viscous experiments in map view: (c-d) experiments P3 and P7 (reference extension velocity experiments, without seed), (e) Exp. P10 (reference extension velocity, with seed), (f) Exp. P9 (40 mm total thickness, high extension velocity of 80 mm/h, no seed). Note that boundary effects are present on both sides of the model, but these are partially invisible due to shadow. (g) Schematic section depicting the interpreted internal structures of experiment P9 (high extension velocity experiment) from surface data and the topography of the viscous material after removal of the sand at the end of the model run. Note the two VDs and that the base plates are 3 mm thick

Final top views of brittle-only conveyor base experiments



Final top views of brittle-viscous conveyor base experiments

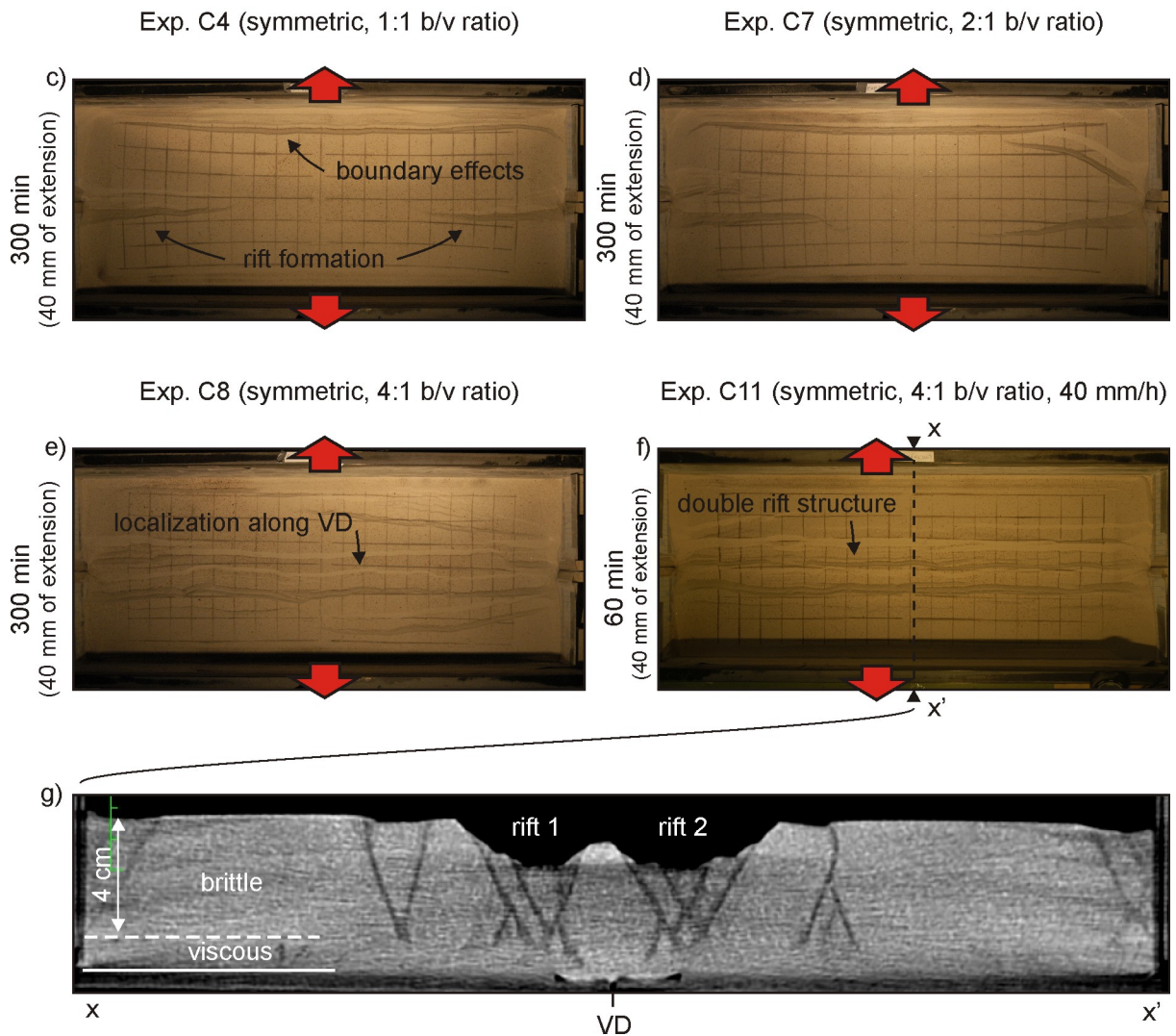
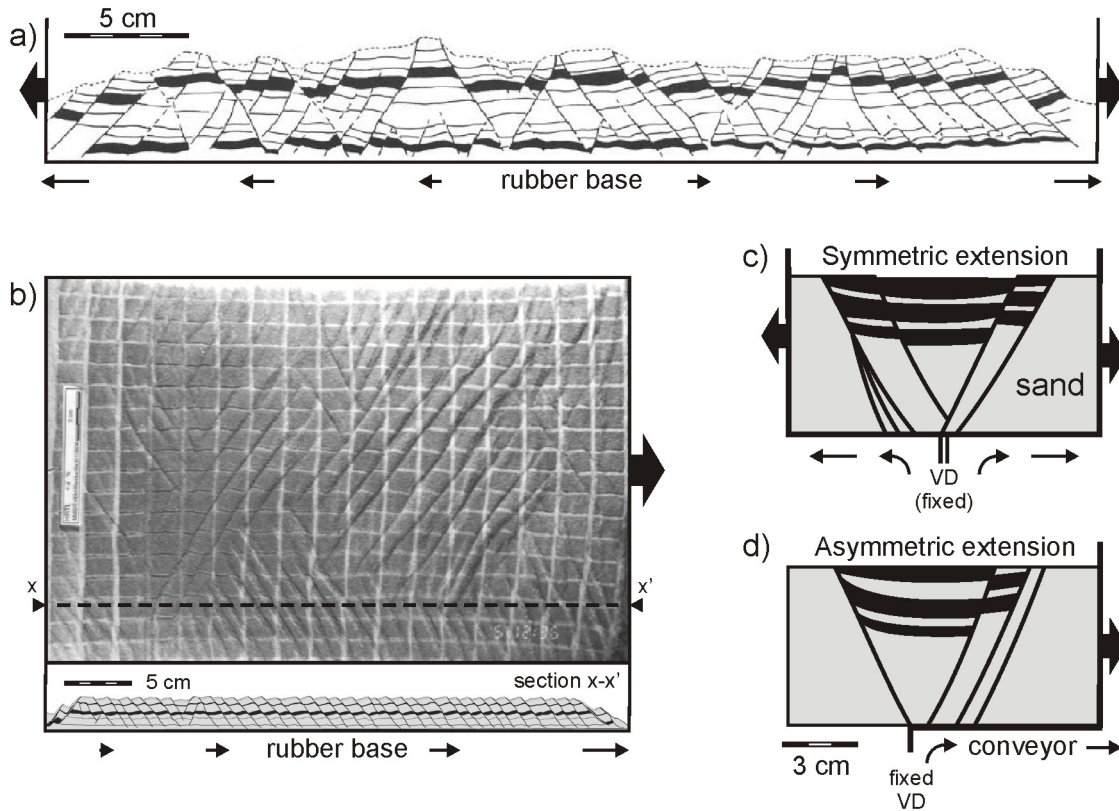
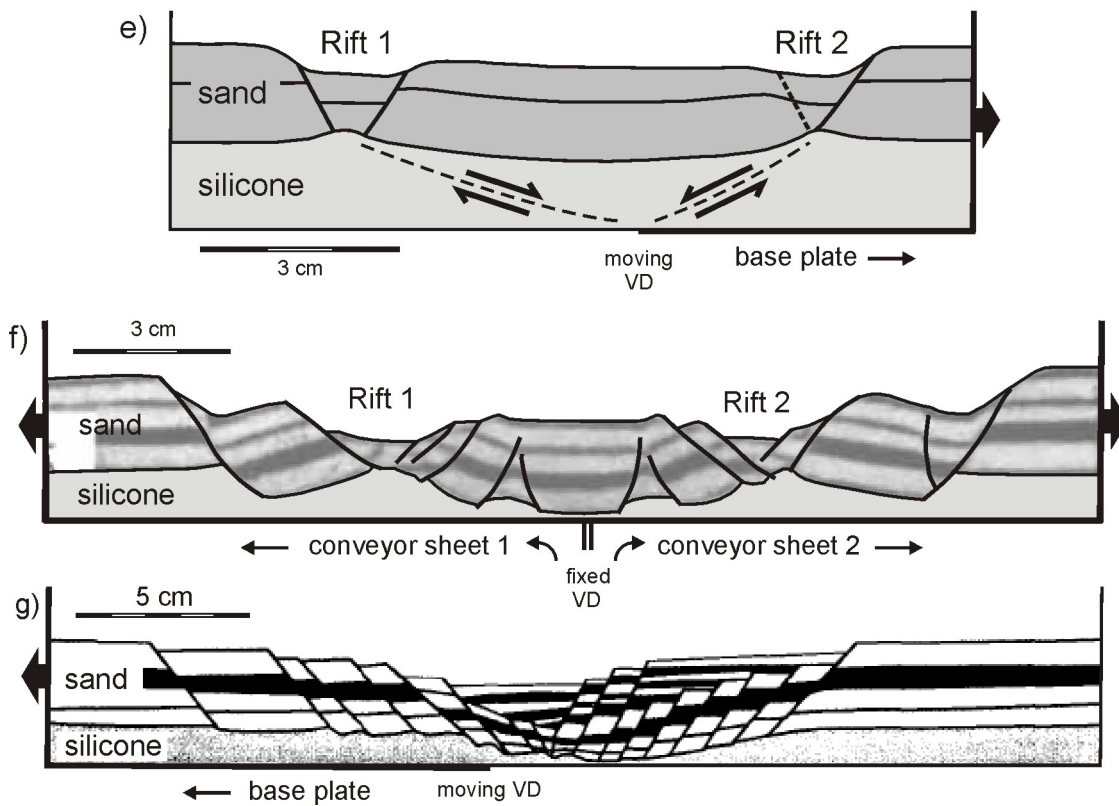


Fig. 9. Overview of conveyor base results. Top views depicting the final surface structures of (a, b) brittle-only experiments C1 and C3, (c, d) brittle-viscous Exp. C4 (reference layering and extension velocity), (d) model C7 (reference extension velocity, brittle-to-viscous ratio: 2), (e) Exp. C8 (reference extension velocity, brittle-to-viscous ratio: 4) and (f) Exp. C11 (elevated extension velocity: 40mm/h, brittle-to-viscous ratio: 4). Note that the boundary effects (if present) occur on both sides of the model, but may be partially invisible due to shadow. (g) CT section depicting the internal structures of Exp. C11.

Brittle-only examples



Brittle-viscous examples



1539
1540
1541
1542
1543

Fig. 11. Examples of previously published analogue models of extensional tectonics. (a) Cross-section of a brittle-only rubber base model, as used for homogeneous thin-skinned deformation. Note the conjugate fault sets. Adapted from Vendeville et al. (1987) with permission from the Geological Society, London. (b) Top view and cross-section of a brittle-only rubber base model similar to (a), although developing the conjugate fault sets due to extension-perpendicular contraction of the rubber sheet (Poisson effect). Adapted from Bahroudi et al. (2003) with permission from Elsevier. (c-d) Cross-sections of brittle-only conveyor base experiments with symmetric (c) or symmetrical extension (d), both including syn-rift sedimentation. Here the VD may represent a basement structure controlling deformation in the overlying strata. Redrawn after Allemand & Brun (1991) with permission from. (e-g) Cross-sections of brittle-viscous models with a plate base or conveyor belt set-up, with the VD representing a fracture in the strong brittle mantle affecting the overlying crustal analogues. (e) Brittle-viscous plate base model with asymmetric extension, illustrating the relation between the velocity discontinuity (VD) and the two rift basins. Compare with model C11 (Figs. 9f, g, B2). Redrawn (with permission from Elsevier) after Michon & Merle (2003), who investigated the European Cenozoic Rift System and the influence of VDs in a strong upper lithospheric mantle. (f) Symmetric extension model with conveyor set-up and brittle-viscous layering, designed to simulate the influence of a strong mantle on a two-layer crust. Adapted from Tron & Brun (1991) with permission from Elsevier. (g) Brittle-viscous plate base model with asymmetric extension. Note that this experiment includes syn-rift sedimentation and aims to reproduce the North Sea Viking Graben. Modified after Brun & Tron with permission from Elsevier (1993). Black arrows indicate extensional motion. VD: velocity discontinuity.

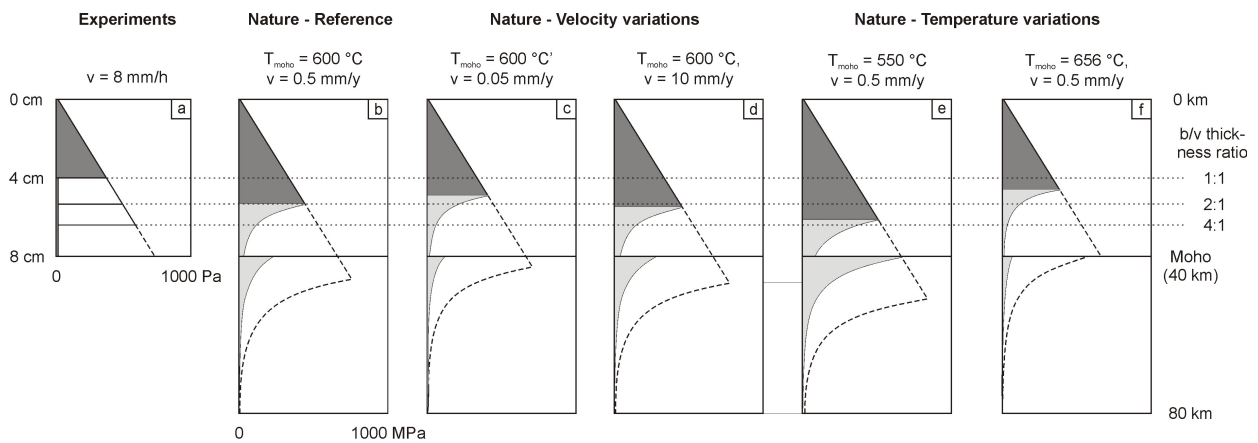
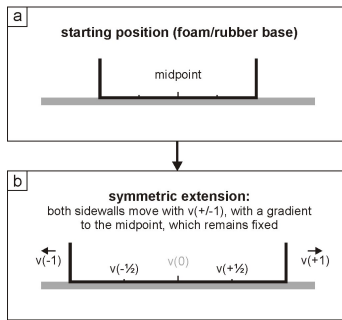


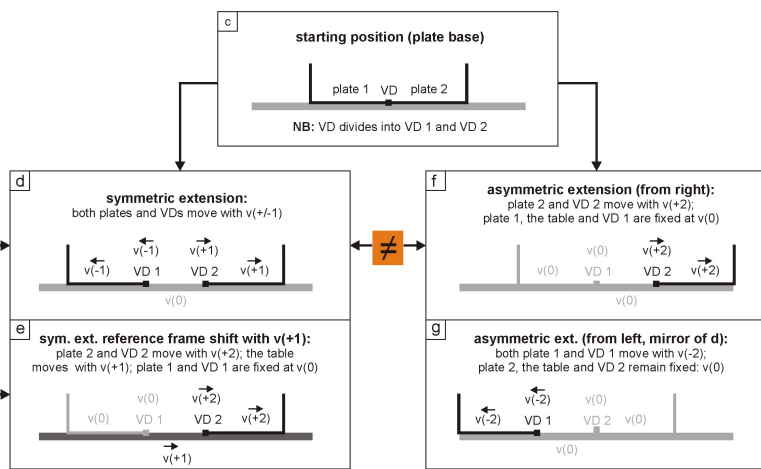
Fig. 12. Strength profiles calculated for our experiments (a) and various natural cases (b-f). Reference values for the natural example are $T_{\text{moho}} = 600 \text{ }^{\circ}\text{C}$ and $v = 0.5 \text{ mm/y}$ (b). Extension velocity variations are shown in (c) and (d) and variations due to different Moho temperatures are depicted in (e) and (f). The crust and mantle flow laws used here are anorthosite dislocation creep (Rybacki et al. 2006) and olivine dislocation creep (Hirth & Kohlstedt 2003). Note that the filled-in profile represents a wet lithosphere, whereas the dotted profiles delineate a dry lithosphere scenario. The horizontal lines indicate various brittle-to viscous ratios (see discussion in text).

Appendix Figures

1. Foam & Rubber base set-ups (F & R series)



2. Plate base set-ups (R series)



3. Conveyor base set-ups (C series)

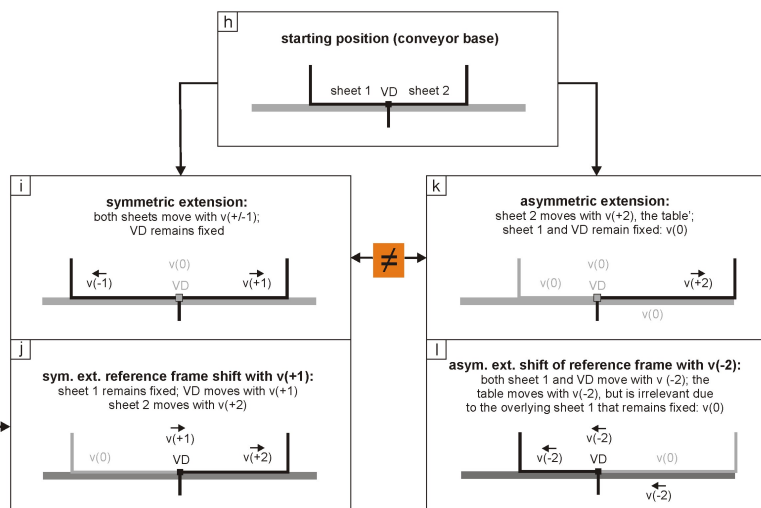
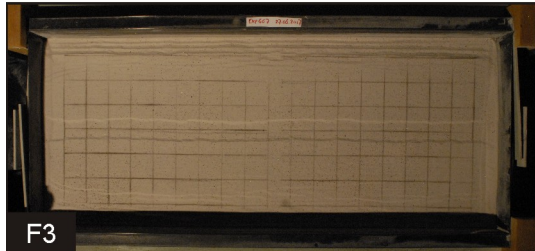
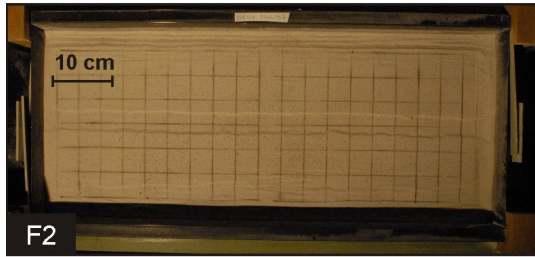


Fig. A1. Schematic overview of relations between experimental set-ups, illustrated with shifts of reference frame (v = velocity, VD = velocity discontinuity). Compare with Fig. 2. (a-b) Foam/rubber base set-ups, in which the base induces a extension gradient. (c-g) Plate base set-ups. (h-l) conveyor base models. Shifts of reference frame are used to highlight the direct differences between models. Note that most set-ups fundamentally differ as indicated by the (\neq) sign, except for the asymmetric plate base and conveyor base set-ups (f-g, k-l), which are fundamentally the same. The latter are indicated by the ($=$) sign. Darker colors indicate mobile parts of the set-ups, whereas brighter colors indicate static parts.

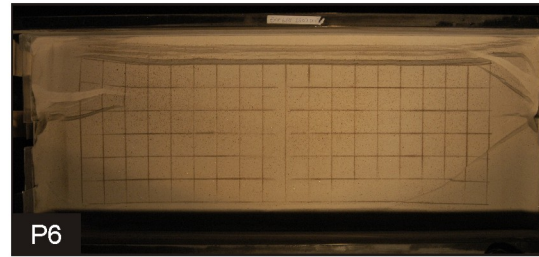
Brittle-only foam base (with seed)



Brittle-viscous foam base (with seed)



Brittle-viscous plate base (no seed)



Brittle-viscous conveyor base (no seed)

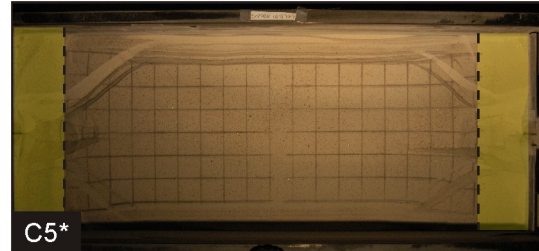
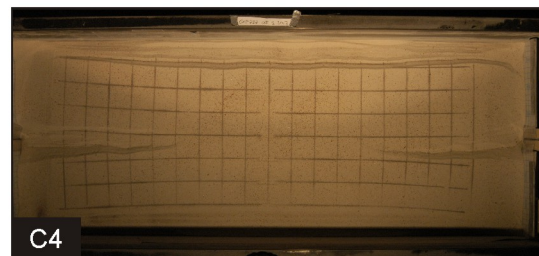
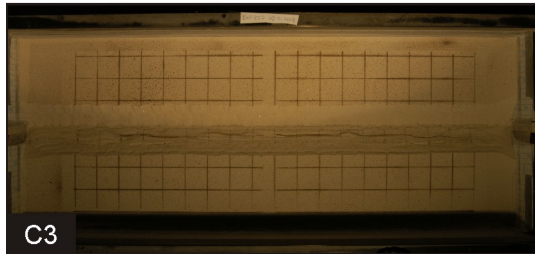
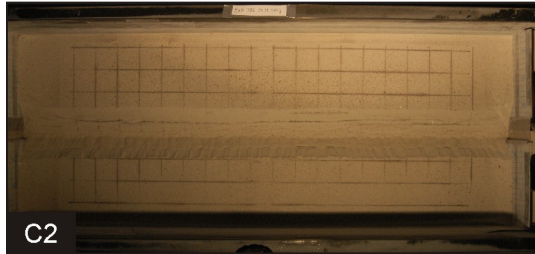
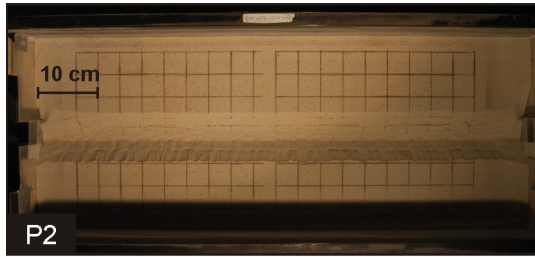
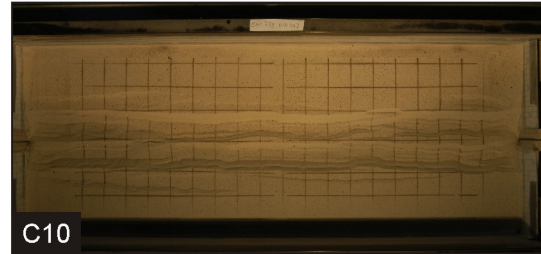
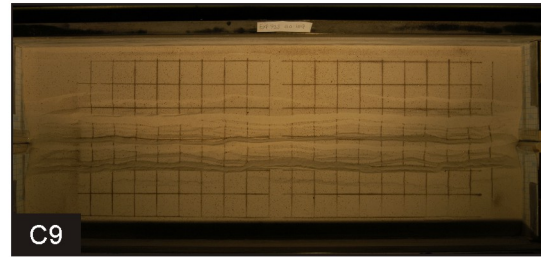


Fig. B1. Reproducibility tests. Final top views of experiments F2-F4 (brittle-only, foam base, with seed), F6 and F7 (brittle-viscous foam base, with seed), P6 and P7 (brittle-viscous plate base models, no seed) and C4-C6 (brittle-viscous conveyor base, no seed). Note that C5* and C6** were attempts to decrease boundary effects by replacing part of the basal viscous layer with sand (transparent overlay) or adding a lubricant (hand soap) along the short ends of the set-up, respectively. The former however increased boundary effects, whereas the latter did not significantly change surface structures and was therefore halted after 2 hours. Extension velocities are 8 mm/h in all cases.

Brittle-only asymmetric plate/conveyor base



Brittle-visc. conv. base (4:1 b/v ratio, high v)



Brittle-viscous plate/conveyor base (high velocity)

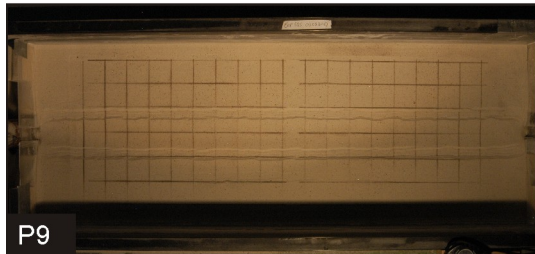


Fig. B2. Reproducibility tests. Final top views of experiments P2, C2 and C3 (brittle-only asymmetric plate base [P] and conveyor base [C]), C9-C11 (brittle-viscous conveyor base models, 4:1 brittle-viscous thickness ratio, high velocity: 40 mm/h [C10/C11] and 80 mm/h [C9]) and experiments P9 and C12 (brittle-viscous plate base [P] and conveyor base [C], half layer thickness, high extension velocity: 80 mm/h).